

Approximate quantum cloning

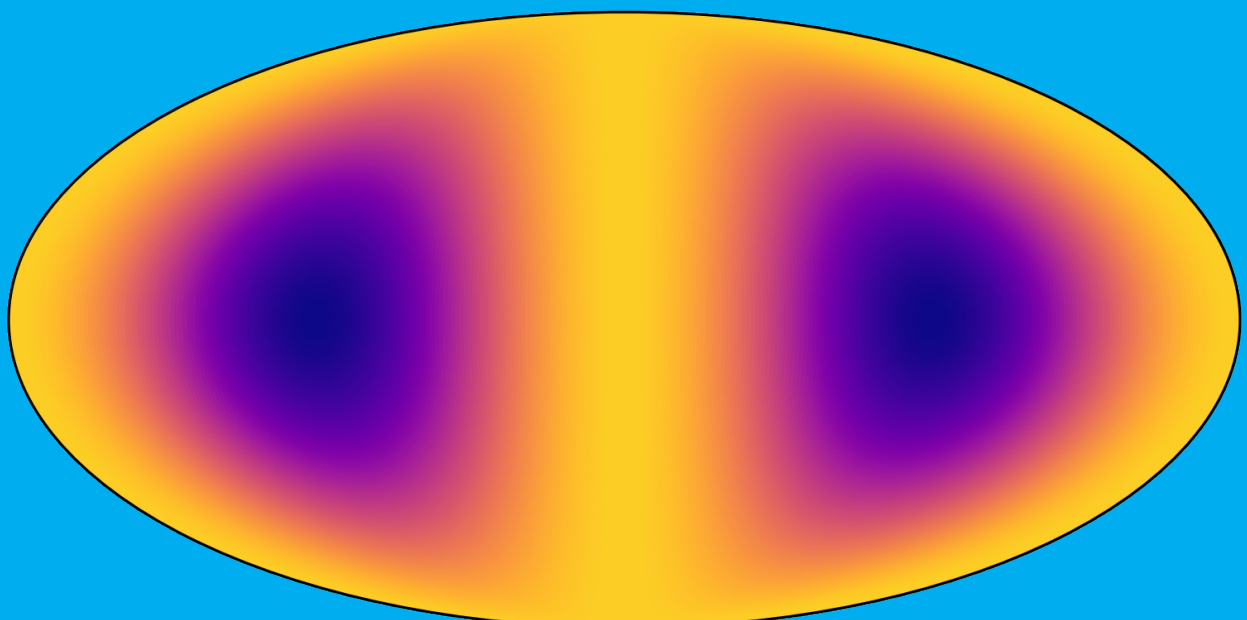
The making of a quantum spy

Quantum Information Project report

Juan Torres

Francesco Zatelli

Yuning Zhang



Contents

1	Introduction	1
2	Approximate quantum cloning	3
2.1	Universal quantum cloning machine	3
2.1.1	Preparation of the state	3
2.1.2	Copying process	4
2.1.3	Single qubit fidelity	5
2.2	Phase covariant quantum cloning machine	6
2.3	Economical phase covariant quantum cloning machine	10
2.4	Quantum cloning and quantum key distribution	12
3	Implementation	13
3.1	Preparation of the input states	13
3.2	Measurement of the fidelity of the copies	14
3.3	Readout calibration	14
3.3.1	Single qubit calibration	15
3.4	Software and hardware details	16
4	Results	19
4.1	Universal quantum cloning machine	19
4.1.1	Sphere	19
4.1.2	Equator	22
4.1.3	BB84 States	24
4.2	Phase covariant quantum cloning machine	25
4.2.1	Sphere	25
4.2.2	Equator	28
4.2.3	BB84 states	31
4.3	Economical phase covariant quantum cloning machine	32
4.3.1	Sphere	32
4.3.2	Equator	32
4.3.3	BB84 states	32
5	Conclusions	33
A	Results without readout correction	35
A.1	Universal quantum cloning machine	35
A.2	Phase covariant quantum cloning machine	35
A.3	Economical phase covariant quantum cloning machine	35
Bibliography		37

Introduction

The no-cloning theorem is a fundamental result of quantum mechanics, which states that a generic quantum state can not be copied exactly [11]. However, imperfect cloning is not forbidden, as was observed by Bužek and Hillery in 1996, who first proposed an approximate quantum cloning machine (QCM) for qubits [3]. Such QCM produces two identical imperfect copies of an arbitrary input state, making use of an extra ancillary qubit. The quality of the copies is independent of the input state, therefore it is known as universal quantum cloning machine (UQCM). Other QCMs were then proposed, for example the phase-covariant quantum cloning machine (PCQCM), which optimally clones the states on an equator of the Bloch sphere [2]. Another category of quantum cloning machines is economical quantum cloning machines (EQCM), which do not use the extra ancillary qubit [8].

Quantum cloning is of particular interest in the context of quantum key distribution (QKD) [10]. The security of QKD protocols relies on the no-cloning theorem, therefore a QCM is a suitable means of attack. An eavesdropper could intercept the state that Alice is sending to Bob, clone it approximately and send the imperfect copy to Bob. Eve could store her copies and wait for Bob to reveal the basis he has performed each measurement. Afterwards, she could measure her qubits in the same basis as Bob, obtaining a string of outcomes equivalent to Bob's one. Since, the copy sent to Bob is not exact, Alice and Bob would find some missing correlations in their bit strings during the sifting procedure. Nonetheless, the errors introduced by the QCM could be confused with generic noise (inevitable in a real setting) and the eavesdropper could go unnoticed. This is why QKD protocols have a threshold for the maximum error rate tolerated: due to the laws of quantum mechanics, there is a trade-off between the information acquired by Eve and the disturbance introduced while acquiring such information. QCMs could be used to push this information-disturbance trade-off to the limit.

In this project we have implemented an experimental realization of the universal, the phase-covariant and the economical phase-covariant QCMs on the quantum processors available via Quantum Inspire [9] and IBM Quantum Experience [7]. The purpose of the present work is to compare the performances of different backends with each other and with the theoretical expectations, addressing the question of whether current quantum computers could be used as QCMs, focusing in particular on their use for eavesdropping. We considered three different sets of input states in order to evaluate the QCMs: the whole Bloch sphere, the equator of the Bloch sphere in the xz -plane and the BB84 states (i.e. the computational and the Hadamard basis). In each of these cases we have calculated the average fidelity of the two copies. Moreover, we also studied the results calibrating the readout.

The report is structured as follows: in Section 2 we introduce the afore-mentioned QCMs, in Section 3 we discuss the experimental setup with which we have implemented and tested them on real hardware, in Section 4 we examine the obtained results, in Section 5 we draw some conclusions and discuss possible further developments.

2

Approximate quantum cloning

2.1. Universal quantum cloning machine

It is well known that an arbitrary quantum state cannot be copied due to the unitarity of quantum mechanics. Nevertheless, there are several approaches to produce an imperfect quantum copy[2, 3, 6?]. Here, we discuss a well known approach for copying arbitrary quantum states with a maximum possible fidelity of $F = 5/6$. This fidelity was initially found to be a high fidelity for quantum copies[3]. Later studies[10?] found that this is the highest possible fidelity that can be achieved by a quantum copy machine.

Let us start by considering an arbitrary state,

$$|\Psi\rangle_{a_0} = \alpha|0\rangle_{a_0} + \beta|1\rangle_{a_0}. \quad (2.1)$$

We are interested in copy this state using the copy machine devised in Ref. [3]. For such purpose, we require two ancillary registers. The full quantum circuit corresponding to the UQCM contains two stages, as can be seen in Fig. 2.1.

2.1.1. Preparation of the state

The first stage of the UQCM starts before interacting with the input qubit. The two bottom qubits are required to be in an arbitrary state,

$$|\phi\rangle_{a_1 b_1} = C_1|00\rangle + C_2|01\rangle + C_3|10\rangle + C_4|11\rangle. \quad (2.2)$$

For such purpose we use the circuit shown in Fig. 2.2 with an input state $|00\rangle_{a_1 b_1}$.

We analyse each stage of the preparation process. To simplify the notation used, we label $|00\rangle_{a_1 b_1} = |00\rangle$, where the qubit from left to right side is always $a_1 b_1$.

The rotation gate shown in Fig. 2.2 is defined as,

$$R_y(\theta) = \cos(\theta/2)\hat{I} - i\sin(\theta/2)\hat{Y} = \begin{pmatrix} \cos(\theta/2) & -\sin(\theta/2) \\ \sin(\theta/2) & \cos(\theta/2) \end{pmatrix}.$$

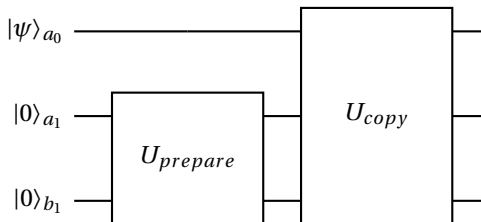


Figure 2.1: General circuit for the universal quantum cloning machine initially presented in Ref. [3].

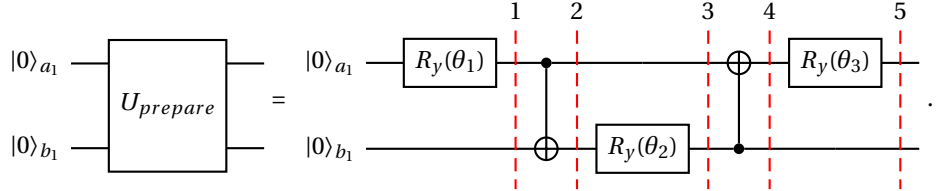


Figure 2.2: Preparation stage of the circuit shown in Fig. 2.1. Each step of the process is labeled.

The evolution of the ancilla qubits along each stage of the circuit is given by,

$$\begin{aligned}
 |\phi_0\rangle &= |00\rangle \\
 |\phi_1\rangle &= (\cos(\theta_1/2)|0\rangle + \sin(\theta_1/2)|1\rangle)|0\rangle \\
 |\phi_2\rangle &= \cos(\theta_1/2)|00\rangle + \sin(\theta_1/2)|11\rangle \\
 |\phi_3\rangle &= \cos(\theta_1/2)|0\rangle(\cos(\theta_2/2)|0\rangle + \sin(\theta_2/2)|1\rangle) + \sin(\theta_1/2)|1\rangle(-\sin(\theta_2/2)|0\rangle + \cos(\theta_2/2)|1\rangle) \\
 &= \cos(\theta_1/2)\cos(\theta_2/2)|00\rangle + \cos(\theta_1/2)\sin(\theta_2/2)|01\rangle \\
 &\quad - \sin(\theta_1/2)\sin(\theta_2/2)|10\rangle + \sin(\theta_1/2)\cos(\theta_2/2)|11\rangle \\
 |\phi_4\rangle &= \cos(\theta_1/2)\cos(\theta_2/2)|00\rangle + \cos(\theta_1/2)\sin(\theta_2/2)|11\rangle \\
 &\quad - \sin(\theta_1/2)\sin(\theta_2/2)|10\rangle + \sin(\theta_1/2)\cos(\theta_2/2)|01\rangle \\
 |\phi_5\rangle &= (\cos(\theta_3/2)|0\rangle + \sin(\theta_3/2)|1\rangle)(\cos(\theta_1/2)\cos(\theta_2/2)|0\rangle + \sin(\theta_1/2)\cos(\theta_2/2)|1\rangle) \\
 &\quad + (-\sin(\theta_3/2)|0\rangle + \cos(\theta_3/2)|1\rangle)(\cos(\theta_1/2)\sin(\theta_2/2)|1\rangle - \sin(\theta_1/2)\sin(\theta_2/2)|0\rangle)
 \end{aligned}$$

After these transformation, we can express it as an arbitrary two-qubit quantum state,

$$|\phi\rangle = C_1|00\rangle + C_2|01\rangle + C_3|10\rangle + C_4|11\rangle. \quad (2.3)$$

From which we can observe that the coefficients depend explicitly on the rotation angles as,

$$C_1 = \sin(\theta_1/2)\sin(\theta_2/2)\sin(\theta_3/2) + \cos(\theta_1/2)\cos(\theta_2/2)\cos(\theta_3/2) \quad (2.4)$$

$$C_2 = \sin(\theta_1/2)\cos(\theta_2/2)\cos(\theta_3/2) - \cos(\theta_1/2)\sin(\theta_2/2)\sin(\theta_3/2) \quad (2.5)$$

$$C_3 = \cos(\theta_1/2)\cos(\theta_2/2)\sin(\theta_3/2) - \sin(\theta_1/2)\sin(\theta_2/2)\cos(\theta_3/2) \quad (2.6)$$

$$C_4 = \sin(\theta_1/2)\cos(\theta_2/2)\sin(\theta_3/2) + \cos(\theta_1/2)\sin(\theta_2/2)\cos(\theta_3/2) \quad (2.7)$$

The angles used to produce an arbitrary state have been previously studied in Ref. [3?]. The following angles were used for the preparation of the state given in Eq. (2.9), that is,

$$\cos(2\theta_1) = \frac{1}{\sqrt{5}}, \quad \cos(2\theta_2) = \frac{\sqrt{5}}{3}, \quad \cos(2\theta_3) = \frac{2}{\sqrt{5}}. \quad (2.8)$$

2.1.2. Copying process

The copying process can be described as controlled entanglement between the input and prepared qubits. Once the ancilla qubits are prepared in the desired input state, we proceed to apply the copy machine. The circuit corresponding to the copy process can be observed in the following circuit, where the prepared initial state and the input state that we consider are given respectively by,

$$|\phi\rangle_{a_1, b_1}^{(prep)} = \frac{1}{\sqrt{6}}(2|00\rangle + |01\rangle + |11\rangle), \quad |\psi\rangle_{a_0}^{(in)} = \alpha|0\rangle + \beta|1\rangle. \quad (2.9)$$

We consider that the input state of the copy machine is $|\Psi_0\rangle = |\psi\rangle_{a_0}^{(in)}|\phi\rangle_{a_1, b_1}^{(prep)}$. Then, it will transform in

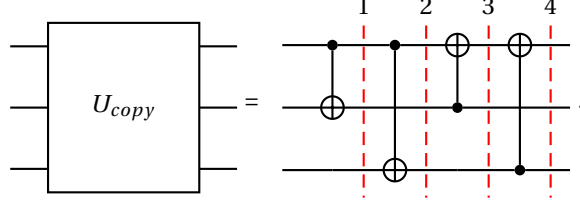


Figure 2.3: Copying stage of the circuit shown in Fig. 2.1. Each step of the process is labeled.

each stage of the copy process as,

$$\begin{aligned}
 |\Psi_1\rangle &= \frac{\alpha}{\sqrt{6}}|0\rangle(2|00\rangle + |01\rangle + |11\rangle) + \frac{\beta}{\sqrt{6}}|1\rangle(2|10\rangle + |11\rangle + |01\rangle) \\
 |\Psi_2\rangle &= \frac{\alpha}{\sqrt{6}}|0\rangle(2|00\rangle + |01\rangle + |11\rangle) + \frac{\beta}{\sqrt{6}}|1\rangle(2|11\rangle + |10\rangle + |00\rangle) \\
 &= \sqrt{\frac{2}{3}}(\alpha|000\rangle + \beta|111\rangle) + \frac{1}{\sqrt{6}}(\alpha|001\rangle + \alpha|011\rangle + \beta|110\rangle + \beta|100\rangle) \\
 |\Psi_3\rangle &= \sqrt{\frac{2}{3}}(\alpha|000\rangle + \beta|011\rangle) + \frac{1}{\sqrt{6}}(\alpha|001\rangle + \alpha|111\rangle + \beta|010\rangle + \beta|100\rangle) \\
 |\Psi_4\rangle &= \sqrt{\frac{2}{3}}(\alpha|000\rangle + \beta|111\rangle) + \frac{1}{\sqrt{6}}(\alpha|101\rangle + \alpha|011\rangle + \beta|010\rangle + \beta|100\rangle) \\
 &= \left(\sqrt{\frac{2}{3}}\alpha|00\rangle + \beta\frac{1}{\sqrt{6}}(|10\rangle + |01\rangle) \right)|0\rangle + \left(\sqrt{\frac{2}{3}}\beta|11\rangle + \frac{1}{\sqrt{6}}\alpha(|10\rangle + |01\rangle) \right)|1\rangle.
 \end{aligned}$$

The final state, after the application of the copy machine, can be written as,

$$|\Psi\rangle = |\chi_0\rangle|0\rangle + |\chi_1\rangle|1\rangle = \left(\sqrt{\frac{2}{3}}\alpha|00\rangle + \sqrt{\frac{1}{3}}\beta|\Phi_+\rangle \right)|0\rangle + \left(\sqrt{\frac{2}{3}}\beta|11\rangle + \sqrt{\frac{1}{3}}\alpha|\Phi_+\rangle \right)|1\rangle, \quad (2.10)$$

where we have defined,

$$|\chi_0\rangle = \sqrt{\frac{2}{3}}\alpha|00\rangle + \sqrt{\frac{1}{3}}\beta|\Phi_+\rangle = \sqrt{\frac{2}{3}}\alpha|00\rangle + \sqrt{\frac{1}{6}}\beta|01\rangle + \sqrt{\frac{1}{6}}\beta|10\rangle \quad (2.11)$$

$$|\chi_1\rangle = \sqrt{\frac{2}{3}}\beta|11\rangle + \sqrt{\frac{1}{3}}\alpha|\Phi_+\rangle = \sqrt{\frac{2}{3}}\beta|11\rangle + \sqrt{\frac{1}{6}}\alpha|01\rangle + \sqrt{\frac{1}{6}}\alpha|10\rangle. \quad (2.12)$$

Note that both $|\chi_0\rangle$ and $|\chi_1\rangle$ are invariant under exchange of the qubits. This implies that the density matrices associated to the copy and to the original qubit are identical, $\rho_{a_0} = \rho_{a_1}$. Then, when we calculate the fidelity of these qubits, they would retrieve the same result.

2.1.3. Single qubit fidelity

After performing the copying process, the input qubit is separated from the copying qubits and measured in a different laboratory. Thus, they can only have access to the partial system involving only the input qubit. To determine the properties of this qubit, we trace out the qubits associated to the copying process, and express the density matrix of the system only in terms of the input qubit. That is,

$$\begin{aligned}
\rho_{a_0} &= \text{Tr}_{a_1}[|\chi_0\rangle\langle\chi_0| + |\chi_1\rangle\langle\chi_1|] = \text{Tr}_{a_1}[|\chi_0\rangle\langle\chi_0|] + \text{Tr}_{a_1}[|\chi_1\rangle\langle\chi_1|] \\
&= \frac{2}{3}|\alpha|^2|0\rangle\langle 0| + \frac{1}{6}|\beta|^2|0\rangle\langle 0| + \frac{1}{6}|\beta|^2|1\rangle\langle 1| + \frac{1}{3}\alpha\beta^*|0\rangle\langle 1| + \frac{1}{3}\alpha^*\beta|1\rangle\langle 0| \\
&\quad + \frac{2}{3}|\beta|^2|1\rangle\langle 1| + \frac{1}{6}|\alpha|^2|0\rangle\langle 0| + \frac{1}{6}|\alpha|^2|1\rangle\langle 1| + \frac{1}{3}\alpha\beta^*|0\rangle\langle 1| + \frac{1}{3}\alpha^*\beta|1\rangle\langle 0| \\
&= \frac{5}{6}|\alpha|^2|0\rangle\langle 0| + \frac{5}{6}|\beta|^2|1\rangle\langle 1| + \frac{1}{6}|\beta|^2|0\rangle\langle 0| + \frac{1}{6}|\alpha|^2|1\rangle\langle 1| + \frac{2}{3}\alpha\beta^*|0\rangle\langle 1| + \frac{2}{3}\alpha^*\beta|1\rangle\langle 0| \\
&= \frac{5}{6}|\alpha|^2|0\rangle\langle 0| + \frac{5}{6}|\beta|^2|1\rangle\langle 1| + \frac{5}{6}\alpha\beta^*|0\rangle\langle 1| + \frac{5}{6}\alpha^*\beta|1\rangle\langle 0| \\
&\quad - \frac{1}{6}\alpha\beta^*|0\rangle\langle 1| - \frac{1}{6}\alpha^*\beta|1\rangle\langle 0| + \frac{1}{6}|\beta|^2|0\rangle\langle 0| + \frac{1}{6}|\alpha|^2|1\rangle\langle 1| \\
&= \frac{5}{6}|\psi\rangle\langle\psi| + \frac{1}{6}|\psi_\perp\rangle\langle\psi_\perp|.
\end{aligned}$$

Finally, the density matrix of the input qubit, or the first copying qubit, is given by,

$$\rho_{a_0} = \frac{5}{6}|\psi\rangle\langle\psi| + \frac{1}{6}|\psi_\perp\rangle\langle\psi_\perp| = \frac{1}{2}\left(\mathbf{I} + \frac{2}{3}\hat{m}\cdot\vec{\sigma}\right), \quad (2.13)$$

where $|\psi\rangle = \alpha|0\rangle + \beta|1\rangle$ is the input state aligned along \hat{m} , and $|\psi_\perp\rangle = \beta^*|0\rangle - \alpha^*|1\rangle$ is its orthogonal state. Then, we calculate the fidelity of a pure state with a mixed state, which is given by,

$$F(|\psi\rangle, \rho) = \langle\psi|\rho|\psi\rangle. \quad (2.14)$$

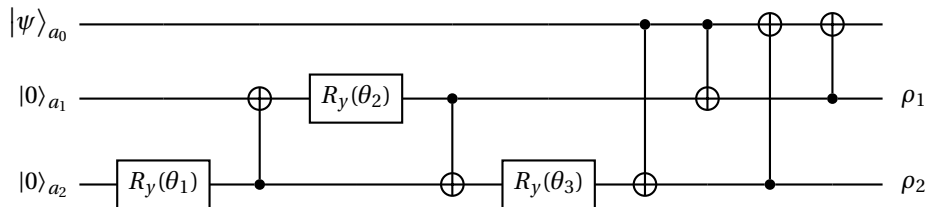
In our case, the fidelity of the output copies is:

$$F(|\psi\rangle, \rho_{a_0}) = \langle\psi|\rho_{a_0}|\psi\rangle = \frac{5}{6} = F(|\psi\rangle, \rho_{a_1}). \quad (2.15)$$

This is the maximum possible fidelity that can be obtained when one tries to copy an arbitrary quantum state. The final state is the same for the input qubit, and for the first copying qubit. One can think of the copying process as the interaction of the input qubit with an environment modeled by the copying qubits. After the copying process, the initial information is evenly distributed between the environment and the input qubit. This copy machine makes copies that are aligned along the same direction as the input qubit, but their magnitude decreases by a factor 2/3 as shown in Ref. [10].

2.2. Phase covariant quantum cloning machine

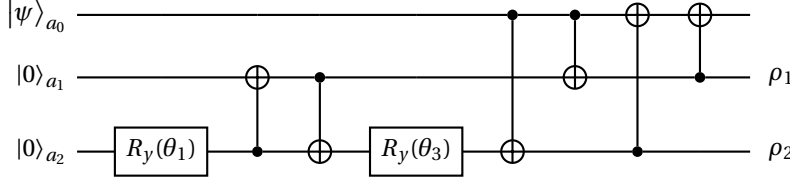
A phase covariant quantum cloning machine (PCQCM) is a QCM optimized to clone states on an equator of the Bloch sphere. The circuit for the optimal PCQCM proposed in [6] is similar to the one for the UQCM, but the output copies are on the registers of the ancillae:



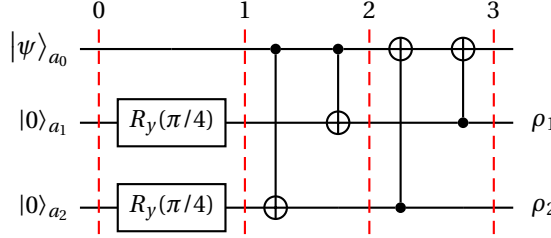
The only significant difference is the preparation of the two ancillae. In this case, different angles of rotation are used. In order to optimally clone the states on the xz equator, the following angles have to be chosen:

$$\theta_1 = \theta_3 = \frac{\pi}{4}, \quad \theta_2 = 0.$$

Hence, the circuit above can be rewritten removing the rotation $R_y(\theta_2)$:



The first two CNOT gates in this circuit act as a SWAP gate (because $|0\rangle_{a1}$ is the input state of the central qubit). Hence, these two CNOT gates are not necessary. It is possible to ignore them, provided that $R_y(\theta_3)$ is moved to the second qubit. Since $\theta_1 = \theta_3 = \theta = \frac{\pi}{4}$, the final circuit is obtained



We have managed to greatly simplify the circuit. We have removed 5 CNOT gates from the circuit that we were using on real quantum processors with linear connectivity: the 2 CNOT gates mentioned here and the 3 CNOT gates that were necessary in order to implement the SWAP gate that was necessary to respect the connectivity constraints. With this new circuit, only the top qubit has to be able to connect to the other two qubits. As a final observation, since this circuit is much more simple than the one for the universal QCM, the average fidelity over the whole Bloch sphere could be greater in this case than with the universal QCM.

We will now show, step by step, that this circuit does clone states on the xz -equator. We consider a generic input state

$$|\psi\rangle = \cos(\theta/2)|0\rangle + e^{i\phi}\sin(\theta/2)|1\rangle,$$

therefore the initial state of the full circuit is

$$|\Psi_0\rangle = |\psi\rangle_{a_0} |0\rangle_{a_1} |0\rangle_{a_2}.$$

Each ancilla, after the rotation, is

$$R_y(\pi/4)|0\rangle = \cos(\pi/8)|0\rangle - \sin(\pi/8)|1\rangle.$$

Hence, the two ancilla are prepared in the following state:

$$\begin{aligned} |\phi\rangle &= (\cos(\pi/8)|0\rangle + \sin(\pi/8)|1\rangle)(\cos(\pi/8)|0\rangle + \sin(\pi/8)|1\rangle) = \\ &= \cos^2(\pi/8)|00\rangle + \cos(\pi/8)\sin(\pi/8)(|01\rangle + |10\rangle) + \sin^2(\theta)|11\rangle. \end{aligned}$$

Right before the CNOT gates, the state of the three qubits is:

$$\begin{aligned} |\Psi_1\rangle &= (\cos(\theta/2)|0\rangle + e^{i\phi}\sin(\theta/2)|1\rangle)(\cos(\pi/8)|0\rangle + \sin(\pi/8)|1\rangle)(\cos(\pi/8)|0\rangle + \sin(\pi/8)|1\rangle) = \\ &= \cos(\theta/2)\cos^2(\pi/8)|000\rangle + e^{i\phi}\sin(\theta/2)\cos^2(\pi/8)|100\rangle \\ &\quad + \cos(\theta/2)\sin(\pi/8)\cos(\pi/8)|010\rangle + e^{i\phi}\sin(\theta/2)\sin(\pi/8)\cos(\pi/8)|110\rangle \\ &\quad + \cos(\theta/2)\cos(\pi/8)\sin(\pi/8)|001\rangle + e^{i\phi}\sin(\theta/2)\cos(\pi/8)\sin(\pi/8)|101\rangle \\ &\quad + \cos(\theta/2)\sin^2(\pi/8)|011\rangle + e^{i\phi}\sin(\theta/2)\sin^2(\pi/8)|111\rangle. \end{aligned}$$

After applying the first two CNOT gates:

$$\begin{aligned} |\Psi_2\rangle &= \cos(\theta/2)\cos^2(\pi/8)|000\rangle + e^{i\phi}\sin(\theta/2)\cos^2(\pi/8)|111\rangle \\ &\quad + \cos(\theta/2)\sin(\pi/8)\cos(\pi/8)|010\rangle + e^{i\phi}\sin(\theta/2)\sin(\pi/8)\cos(\pi/8)|101\rangle \\ &\quad + \cos(\theta/2)\cos(\pi/8)\sin(\pi/8)|001\rangle + e^{i\phi}\sin(\theta/2)\cos(\pi/8)\sin(\pi/8)|110\rangle \\ &\quad + \cos(\theta/2)\sin^2(\pi/8)|011\rangle + e^{i\phi}\sin(\theta/2)\sin^2(\pi/8)|100\rangle. \end{aligned}$$

After applying the last two CNOT gates:

$$\begin{aligned} |\Psi_3\rangle = & \cos(\theta/2) \cos^2(\pi/8) |000\rangle + e^{i\phi} \sin(\theta/2) \cos^2(\pi/8) |111\rangle \\ & + \cos(\theta/2) \sin(\pi/8) \cos(\pi/8) |110\rangle + e^{i\phi} \sin(\theta/2) \sin(\pi/8) \cos(\pi/8) |001\rangle \\ & + \cos(\theta/2) \cos(\pi/8) \sin(\pi/8) |101\rangle + e^{i\phi} \sin(\theta/2) \cos(\pi/8) \sin(\pi/8) |010\rangle \\ & + \cos(\theta/2) \sin^2(\pi/8) |011\rangle + e^{i\phi} \sin(\theta/2) \sin^2(\pi/8) |100\rangle. \end{aligned}$$

The above state is invariant under the exchange of the second and third qubits, where the copies are made. This means that the single qubit states of the two copies are the same, i.e.:

$$\rho_1 = \rho_2 \quad \text{where} \quad \rho_1 = \text{Tr}_{a_0, a_2}[|\Psi_3\rangle\langle\Psi_3|], \quad \rho_2 = \text{Tr}_{a_0, a_1}[|\Psi_3\rangle\langle\Psi_3|].$$

In order to calculate the expected fidelity of the copies (we will consider the copy ρ_1), we first isolate the qubits a_0 and a_2 :

$$\begin{aligned} |\Psi_3\rangle = & |0\rangle (\cos(\theta/2) \cos^2(\pi/8) |0\rangle + e^{i\phi} \sin(\theta/2) \cos(\pi/8) \sin(\pi/8) |1\rangle) |0\rangle \\ & + |0\rangle (e^{i\phi} \sin(\theta/2) \sin(\pi/8) \cos(\pi/8) |0\rangle + \cos(\theta/2) \sin^2(\pi/8) |1\rangle) |1\rangle \\ & + |1\rangle (e^{i\phi} \sin(\theta/2) \sin^2(\pi/8) |0\rangle + \cos(\theta/2) \sin(\pi/8) \cos(\pi/8) |1\rangle) |0\rangle \\ & + |1\rangle (\cos(\theta/2) \cos(\pi/8) \sin(\pi/8) |0\rangle + e^{i\phi} \sin(\theta/2) \cos^2(\pi/8) |1\rangle) |1\rangle. \end{aligned}$$

The single copy fidelity is then (θ and ϕ are the angles on the Bloch sphere of the input state):

$$\begin{aligned} F(\theta, \phi) = & \langle \psi | \rho_1 | \psi \rangle = \langle \psi | \text{Tr}_{a_0, a_2}[|\Psi_3\rangle\langle\Psi_3|] | \psi \rangle = \\ = & (\cos^2(\theta/2) \cos^2(\pi/8) + \sin^2(\theta/2) \cos(\pi/8) \sin(\pi/8))^2 \\ & + |e^{i\phi} \cos(\theta/2) \sin(\theta/2) \sin(\pi/8) \cos(\pi/8) + e^{-i\phi} \sin(\theta/2) \cos(\theta/2) \sin^2(\pi/8)|^2 \\ & + |e^{i\phi} \cos(\theta/2) \sin(\theta/2) \sin^2(\pi/8) + e^{-i\phi} \sin(\theta/2) \cos(\theta/2) \sin(\pi/8) \cos(\pi/8)|^2 \\ & + (\cos^2(\theta/2) \cos(\pi/8) \sin(\pi/8) + \sin^2(\theta/2) \cos^2(\pi/8))^2. \end{aligned}$$

The fidelity can be computed analytically. The final result is:

$$F(\theta, \phi) = \frac{3(4 - \sqrt{2}) + (3\sqrt{2} - 4)[\cos(2\phi) + \cos(2\theta)(1 - \cos(2\phi))]}{16(2 - \sqrt{2})}. \quad (2.16)$$

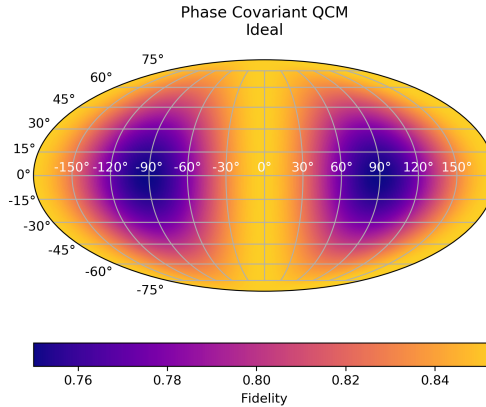


Figure 2.4: Caption

It is possible to observe that if $\phi = 0$ is set, the fidelity becomes a constant:

$$F(\theta, 0) = \frac{3(4 - \sqrt{2}) + (3\sqrt{2} - 4)}{16(2 - \sqrt{2})} = \frac{8}{16(2 - \sqrt{2})} = \frac{1}{2} \frac{2 + \sqrt{2}}{2} = \frac{1}{2} + \frac{1}{\sqrt{8}}.$$

Therefore, for input states on the xz -equator, the fidelity of the PCQCM is:

$$F_{\text{equator}}^{\text{ideal}} = \frac{1}{2} + \frac{1}{\sqrt{8}} \approx 0.854. \quad (2.17)$$

As discussed in [2] this is the optimal fidelity for a PCQCM. Moreover, this is the optimal result attainable also when trying to maximize the fidelity for BB84 input states. Indeed, the optimization over the two different sets of input states is equivalent and leads therefore to the same result [2].

It might be of some interest to consider the performances of the PCQCM over the whole Bloch sphere. The average fidelity over the Bloch sphere S is (integrating over solid angle):

$$\bar{F} = \frac{1}{\int_S d\Omega} \int_S F(\Omega) d\Omega = \frac{1}{4\pi} \int_0^{2\pi} \int_0^\pi F(\theta, \phi) \sin(\theta) d\theta d\phi = \frac{7+2\sqrt{2}}{12} \approx 0.819. \quad (2.18)$$

The standard deviation can be calculated similarly:

$$\sigma_F = \sqrt{\bar{F}^2 - \bar{F}^2} = \frac{1}{6} \sqrt{\frac{3-2\sqrt{2}}{5}} \approx 0.031. \quad (2.19)$$

We conclude that when considering the PCQCM over the whole Bloch sphere, it is not too far from the optimal bound of the UQCM (which was $F = 5/6 \approx 0.833$). This could have some interesting consequences: since we managed to greatly simplify its circuit, the PCQCM could turn to be better than the UQCM when using real hardware, in contrast with what is expected theoretically. A similar analysis regarding the performances of a real QCM was carried out in [4] in the context of economical QCMs.

Rotated PCQCM

The found expression for the fidelity is rather complicated. When considering a PCQCM that optimally clones the states on the xy -equator, the expression simplifies. It is possible to obtain the fidelity for an arbitrary state on the Bloch sphere starting from the expression previously found, without analyzing a new circuit. Given a point (θ, ϕ) on the Bloch sphere, we want to find the coordinates (θ', ϕ') of such point after a rotation of $\pi/2$ about the x -axis is performed. Indeed, such rotation transforms the xy -equator into the xz -equator.

We start considering a generic vector on a sphere of unit radius:

$$\boldsymbol{v} = \begin{pmatrix} \sin(\theta) \cos(\phi) \\ \sin(\theta) \sin(\phi) \\ \cos(\phi) \end{pmatrix}.$$

An arbitrary rotation about the x -axis in a 3D Euclidean space is given by:

$$R_x(\alpha) = \begin{pmatrix} 1 & 0 & 0 \\ 0 & \cos(\alpha) & -\sin(\alpha) \\ 0 & \sin(\alpha) & \cos(\alpha) \end{pmatrix}$$

Therefore, if we consider a rotation of $\pi/2$ about the x -axis, the transformed vector is:

$$\boldsymbol{v}' = R_x(\pi/2) \boldsymbol{v} = \begin{pmatrix} 1 & 0 & 0 \\ 0 & 0 & -1 \\ 0 & 1 & 0 \end{pmatrix} \begin{pmatrix} \sin(\theta) \cos(\phi) \\ \sin(\theta) \sin(\phi) \\ \cos(\phi) \end{pmatrix} = \begin{pmatrix} \sin(\theta) \cos(\phi) \\ -\cos(\phi) \\ \sin(\theta) \sin(\phi) \end{pmatrix}.$$

Finally, the new angular coordinates can be calculated:

$$\begin{aligned} \theta' &= \arccos\left(\frac{v'_z}{v'}\right) = \arccos(\sin(\theta) \sin(\phi)) \\ \phi' &= \arctan2(v'_y, v'_x) = \arctan2(-\cos(\phi), \sin(\theta) \cos(\phi)) \end{aligned}$$

The fidelity for a PCQCM that optimally clones the state on the xy -equator is obtained from the one previously found simply changing the variables:

$$F_{xy}(\theta, \phi) = F(\theta'(\theta, \phi), \phi'(\theta, \phi)).$$

After some manipulations, it is possible to obtain the following expression:

$$F_{xy}(\theta, \phi) = \frac{5 + \sqrt{2}}{8} + \frac{1 - \sqrt{2}}{8} \cos(2\theta). \quad (2.20)$$

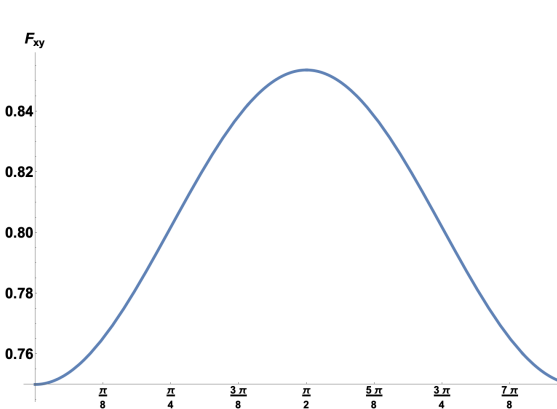


Figure 2.5: Caption (TO FIX)

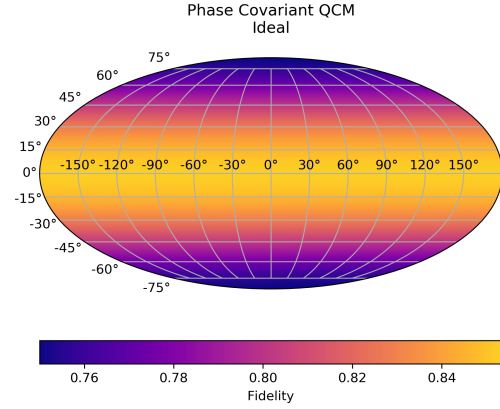


Figure 2.6: Caption (TO FIX)

It is possible to observe that the fidelity does not depend on ϕ , which means that it is constant across sections parallel to the xy -plane. This was not evident with the previous expression, since the sections parallel to the xz -plane do not have such a simple expression.

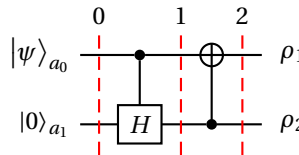
We conclude observing that if $\theta = \pi/2$ (i.e. on the equator), we obtain $F_{xy}(\pi/2, \phi) = \frac{1}{2} + \frac{1}{2\sqrt{2}}$, which is the maximum fidelity achievable. On the other hand, for $\theta = 0$ or $\theta = \pi$, we obtain the minimum fidelity, i.e. $F_{xy}(0, \phi) = 3/4$. Regardless of the equator that is optimally copied, the fidelity is then bounded by

$$\frac{3}{4} \leq F(\theta, \phi) \leq \frac{1}{2} + \frac{1}{2\sqrt{2}}. \quad (2.21)$$

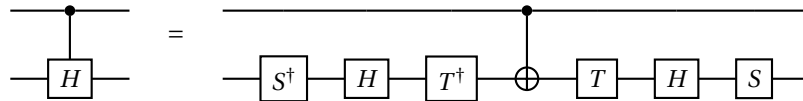
2.3. Economical phase covariant quantum cloning machine

The two previous QCMs used 3 qubits in order to implement the approximate $1 \rightarrow 2$ cloning. One may wonder whether the extra ancillary qubit is necessary. It turns out that in certain cases it is not. The QCMs that only use 2 qubits are known as economical quantum cloning machines (EQCM) [8]. The advantage of EQCMs consists in the fact that their experimental implementation requires less resources. In particular, it was proven that a universal EQCM does not exist [5]. On the other hand, it is possible to build a phase covariant economical quantum cloning machine (PCEQCM), as discussed in the references above.

The circuit to implement a PCEQCM that optimally clones states on the xy -equator is



where the controlled-Hadamard can be rewritten using more elementary gates:



We are going to analyze the circuit considering an arbitrary input state $|\psi\rangle = \cos(\theta/2)|0\rangle + e^{i\phi}\sin(\theta/2)|1\rangle$. The initial state is

$$|\Psi_0\rangle = \cos(\theta/2)|00\rangle + e^{i\phi}\sin(\theta/2)|10\rangle.$$

After applying the controlled-Hadamard gate we obtain

$$|\Psi_1\rangle = \cos(\theta/2)|00\rangle + \frac{1}{\sqrt{2}}e^{i\phi}\sin(\theta/2)|10\rangle + \frac{1}{\sqrt{2}}e^{i\phi}\sin(\theta/2)|11\rangle.$$

Finally, applying the CNOT gate, we get:

$$|\Psi_2\rangle = \cos(\theta/2)|00\rangle + \frac{1}{\sqrt{2}}e^{i\phi}\sin(\theta/2)|10\rangle + \frac{1}{\sqrt{2}}e^{i\phi}\sin(\theta/2)|01\rangle.$$

The above state is invariant under exchange of qubits. This means that the single qubit states are the same, i.e.:

$$\rho_1 = \rho_2 \quad \text{where} \quad \rho_1 = \text{Tr}_{a_1}[|\Psi_2\rangle\langle\Psi_2|], \quad \rho_2 = \text{Tr}_{a_0}[|\Psi_2\rangle\langle\Psi_2|].$$

Since there are only two qubits, it is feasible to calculate the density matrix of the final state of two qubits:

$$\rho_{a_0 a_1} = |\Psi_2\rangle\langle\Psi_2| = \frac{1}{2} \begin{pmatrix} \cos^2\left(\frac{\theta}{2}\right) & \frac{e^{-i\phi}\sin(\theta)}{2\sqrt{2}} & \frac{e^{-i\phi}\sin(\theta)}{2\sqrt{2}} & 0 \\ \frac{e^{i\phi}\sin(\theta)}{2\sqrt{2}} & \frac{1}{2}\sin^2\left(\frac{\theta}{2}\right) & \frac{1}{2}\sin^2\left(\frac{\theta}{2}\right) & 0 \\ \frac{e^{i\phi}\sin(\theta)}{2\sqrt{2}} & \frac{1}{2}\sin^2\left(\frac{\theta}{2}\right) & \frac{1}{2}\sin^2\left(\frac{\theta}{2}\right) & 0 \\ 0 & 0 & 0 & 0 \end{pmatrix}.$$

The reduced density matrix for the copies is:

$$\rho_1 = \text{Tr}_{a_1}[\rho_{a_0 a_1}] = \begin{pmatrix} \cos(\theta) + 3 & \sqrt{2}e^{-i\phi}\sin(\theta) \\ \sqrt{2}e^{i\phi}\sin(\theta) & 1 - \cos(\theta) \end{pmatrix} = \rho_2.$$

When comparing the copies with the input state, the following fidelity is obtained:

$$F_{xy}(\theta, \phi) = \langle \psi | \rho_1 | \psi \rangle = \langle \psi | \rho_2 | \psi \rangle = \frac{1}{8} \left(2\cos(\theta) - (\sqrt{2} - 1)\cos(2\theta) + \sqrt{2} + 5 \right). \quad (2.22)$$

It is possible to observe that the fidelity does not depend on ϕ . Moreover, for $\theta = \frac{\pi}{2}$ (i.e. on the xy -equator):

$$F_{xy}(\pi/2, \phi) = \left(\frac{1}{2} + \frac{1}{2\sqrt{2}} \right) \approx 0.854.$$

This is the same value obtained in the previous section for the PCQCM with the extra ancillary qubit.

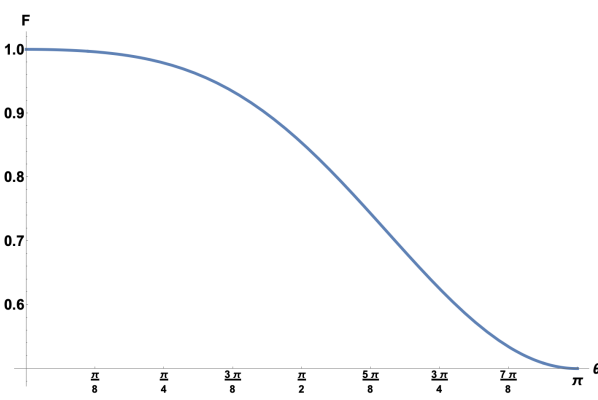


Figure 2.7: Caption (TO FIX)

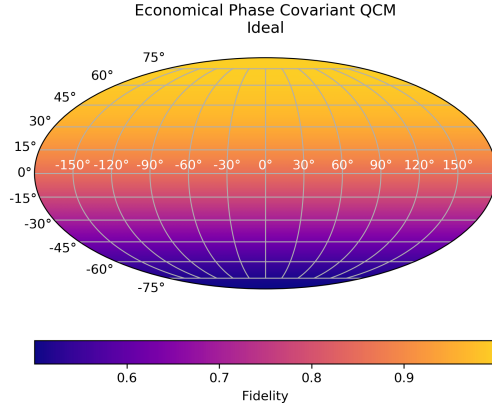


Figure 2.8: Caption (TO FIX)

The average fidelity on the whole Bloch sphere is

$$\bar{F}_{xy} = \frac{1}{\int_S d\Omega} \int_S F_{xy}(\Omega) d\Omega = \frac{1}{2} \int_0^\pi F_{xy}(\theta, \phi) \sin(\theta) d\theta = \frac{7+2\sqrt{2}}{12} \approx 0.819. \quad (2.23)$$

The standard deviation is

$$\sigma_{F_{xy}} = \sqrt{\overline{F}_{xy}^2 - \overline{F}_{xy}^2} = \frac{1}{12} \sqrt{\frac{1}{5} (27 - 8\sqrt{2})} \approx 0.148. \quad (2.24)$$

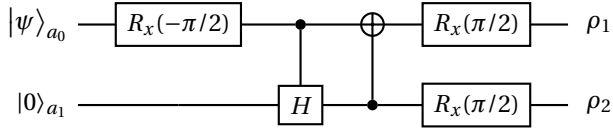
The average fidelity is the same obtained in the previous section for the PCQCM, but in this case the standard deviation is larger. Indeed, the fidelity is bounded by

$$\frac{1}{2} \leq F_{xy}(\theta, \phi) \leq 1, \quad (2.25)$$

where the minimum is reached at $\theta = \pi$ (the South Pole) and the maximum is reached at $\theta = 0$ (the North Pole). This means that the states in the northern hemisphere of the Bloch sphere are cloned better than those on the xy -equator, whereas those in the southern hemisphere are cloned worse.

Rotated EPCQCM

Since we are interested in cloning the states on the xz -equator, we have to perform a rotation before and after the circuit discussed above. The EPCQCM that optimally clones the xz -equator can be implemented using the following circuit:



The fidelity of the copies using the rotated EPCQCM can be calculated as we have shown for the PCQCM. In this case it was more convenient to analyze the circuit for the xy -equator. The fidelity for an EPCQCM that optimally clones the xz -equator is:

$$F(\theta, \phi) = \frac{1}{4} \left(2 + \sqrt{2} - \sin(\theta) \sin(\phi) + (\sqrt{2} - 1) \sin^2(\theta) \sin^2(\phi) \right) \quad (2.26)$$

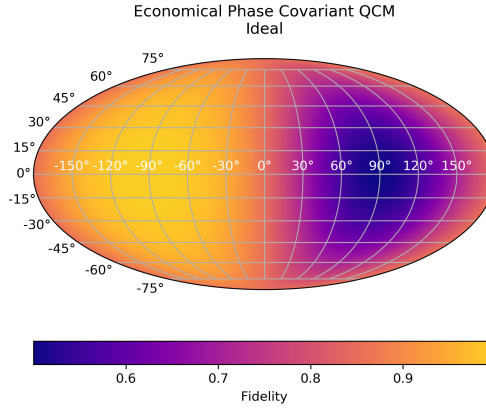


Figure 2.9: Caption

This is the circuit that we have run and the fidelity that we will compare our results with.

2.4. Quantum cloning and quantum key distribution

NB: optimal cloning and optimal eavesdropping are different! When using the 3 qubit phase covariant QCM Eve also has the ancilla, which carries some additional information. See [10] "In summary: without ancilla, Eve can make the best possible guess on the bit sent by Alice (because the machine realizes the optimal phase-covariant cloning) but has very poor information about the result obtained by Bob. Adding the ancilla does not modify the estimation of Alice's bit but allows Eve to deterministically symmetrize her information on Alice and Bob's symbols. However, the two machines are equally good from the point of view of cloning."

3

Implementation

In this section it is explained in detail the procedure we followed in order to assess the performances of the QCMs discussed in the previous section when implemented on real quantum computers. When using noisy hardware, we expect the experimental fidelity to be different from the ideal one all, since the evolution is not unitary anymore. In particular, it should not be assumed the fidelity of the copies to be independent from the input state, for example some gates could work better when acting on certain states. Therefore, two more blocks have to be added to the circuits discussed in the previous section. We have to prepare an arbitrary input state on the Bloch sphere and we have to measure the fidelity of the copies. It is worth mentioning that both the preparation and the fidelity measurement are not required in the normal use of QCMs, they are just a means of testing their performances. It should therefore be taken into account that the additional gates could decrease the quality of the copies because of the greater depth of the run circuits.

This is the outline of a single experiment:

1. Prepare a generic input state $|\psi\rangle = \cos(\theta/2)|0\rangle + e^{i\phi}\sin(\theta/2)|1\rangle$.
2. Run the QCM circuit using the previously prepared input state
3. Measure the fidelity of the copies $F_1(\theta, \phi)$ and $F_2(\theta, \phi)$.

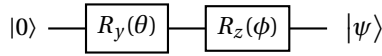
In addition, we have also performed a readout calibration periodically, correcting the classical errors associated to measurements.

The circuits of the QCMs were studied in the previous chapter. In this chapter we are going to analyze the other details specific to our experiments. We are going to explain how we have implemented the preparation of a generic input state, the fidelity measurement and the readout calibration. Finally, we are going to discuss the software and hardware details.

3.1. Preparation of the input states

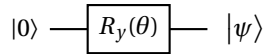
We have prepared a generic state on the Bloch sphere using the following two rotations:

$$|\psi\rangle = R_z(\phi)R_y(\theta)|0\rangle = \cos(\theta/2)|0\rangle + e^{i\phi}\sin(\theta/2)|1\rangle,$$



where θ is the polar angle and ϕ is the azimuthal angle. For the preparation of an input state on the xz -equator, only the rotation about the y axis is needed:

$$|\psi\rangle = R_y(\theta)|0\rangle = \cos(\theta/2)|0\rangle + \sin(\theta/2)|1\rangle.$$



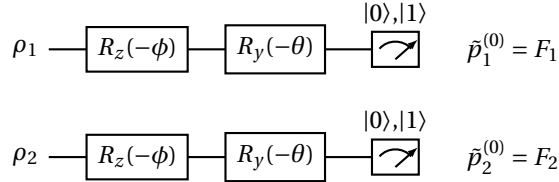
We have considered three sets of input states, namely the Bloch sphere, the xz -equator and the BB84 states ($|0\rangle$, $|1\rangle$, $|+\rangle$ and $|-\rangle$). For the Bloch sphere, we have considered 1000 approximately equidistant point¹. For the xz -equator we have considered 100 equidistant point.

3.2. Measurement of the fidelity of the copies

The fidelity of the two copies can be measured directly. If the input state was $|\psi\rangle$, it is sufficient to perform a measurement in the $\{|\psi\rangle, |\psi_{\perp}\rangle\}$ basis. The fidelity corresponds to the probability of measuring $|\psi\rangle$. Indeed, if the copies are $\rho_{1,2}$ and their fidelities with respect to the input state are $F_{1,2}$:

$$p_{1,2}^{(\psi)} = \text{Tr}[|\psi\rangle\langle\psi| \rho_{1,2}] = \langle\psi|\rho_{1,2}|\psi\rangle = F_{1,2}.$$

Since $|\psi\rangle$ was prepared with the rotation $R_z(\phi)R_y(\theta)$, it follows that a measurement in the $\{|\psi\rangle, |\psi_{\perp}\rangle\}$ basis can be performed implementing the opposite rotation and then measuring in the computational basis.



In the above sketch, we denote with $\tilde{p}_1^{(0)}$ ($\tilde{p}_2^{(0)}$) the probability of finding 0 when measuring the first (second) copy in the computational basis after the rotation. Note that the above probabilities have to be calculated marginalizing over the probability distributions of the qubits we are not interested in. These are the probabilities of obtaining 0 when measuring the first copy, regardless of what happens to the other qubits. Ideally, after

A possible alternative to this way of measuring the fidelity would be to perform a quantum tomography experiment. However, the number of circuits necessary to run would have increased.

3.3. Readout calibration

We considered that a classical error can affect the measurement process. Consider a state of the form $|\psi\rangle = \alpha|0\rangle + \beta|1\rangle$. The expectation value of a measurement along the Z axis is given by $\bar{m} = p_{+1} - p_{-1}$. However, this quantity can be affected by classical errors. In a readout error, a measurement of +1 is transformed to -1 with a probability ϵ_{01} . Similarly for ϵ_{10} . Then, the expectation value will be transformed to,

$$\bar{m} = (1 - 2\epsilon_{10})|\alpha|^2 - (1 - 2\epsilon_{01})|\beta|^2 \quad (3.1)$$

$$= (\epsilon_{01} - \epsilon_{10}) + (1 - \epsilon_{01} - \epsilon_{10})(|\alpha|^2 - |\beta|^2) \quad (3.2)$$

$$= \beta_0 + \beta_1 \langle Z \rangle. \quad (3.3)$$

Note that $|\alpha|^2 = p_{+1}$ and $|\beta|^2 = p_{-1}$ are obtained from measuring the system. Then, we can express the corrected result from Eq. (3.1) as,

$$\langle Z \rangle = \frac{\bar{m} - \beta_0}{\beta_1}. \quad (3.4)$$

Here β_1 and β_2 are the correction coefficients. They are given by,

$$\beta_1 = \frac{1}{2}(p_{+1} + p_{-1}), \quad (3.5)$$

$$\beta_2 = \frac{1}{2}(p_{+1} - p_{-1}). \quad (3.6)$$

They can be used to correct the outcome of future experiments, for example a quantum state tomography. However, they are subject to change during time depending on the details of each device. Furthermore, we

¹Evenly distributing N points on a sphere is not a trivial problem. We have used the Fibonacci spherical lattice method. A detailed explanation can be found at <http://extremelearning.com.au/evenly-distributing-points-on-a-sphere/>.

extend them to correct the probabilities of single qubit measurements. Let \tilde{p}_{+1} and \tilde{p}_{-1} be the corrected probabilities. They satisfy the following conditions,

$$\tilde{p}_{+1} + \tilde{p}_{-1} = 1, \quad (3.7)$$

$$\tilde{p}_{+1} - \tilde{p}_{-1} = \frac{\bar{m} - \beta_0}{\beta_1}. \quad (3.8)$$

The solution of this two equations is given by,

$$\tilde{p}_{+1} = \frac{\beta_0 - \beta_1 + Z}{2\beta_1}, \quad \tilde{p}_{-1} = \frac{\beta_0 + \beta_1 - Z}{2\beta_1}. \quad (3.9)$$

3.3.1. Single qubit calibration

We consider a single qubit tomography to observe the effect of the readout correction. Let us consider a normal singel qubit tomography. We run this experiment in different available experimental backends and correct the results according to Eq. 3.9. The readout parameters were calculated at the begining of the experiment, and then the results were correted. In the following figures, we show the results with and without readout correction.

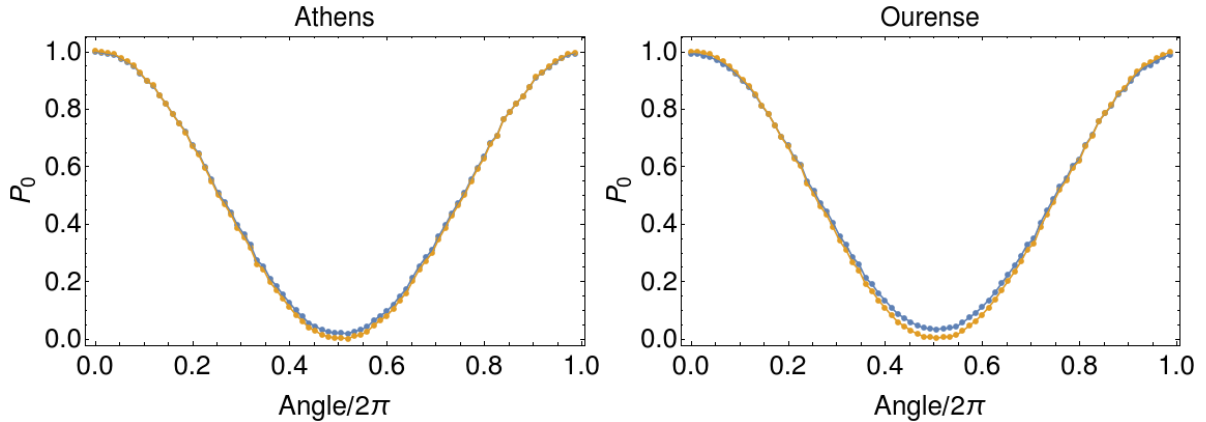


Figure 3.1: Single qubit calibration on Athens and Ourense. Here the blue (orange) line corresponds to the data without (with) readout correction.

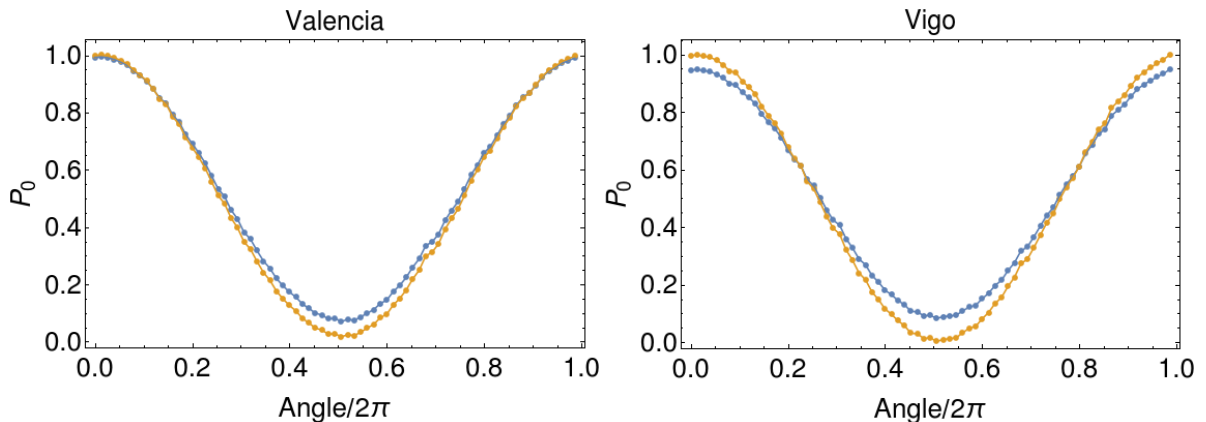


Figure 3.2: Single qubit calibration on Valencia and Vigo. Here the blue (orange) line corresponds to the data without (with) readout correction.

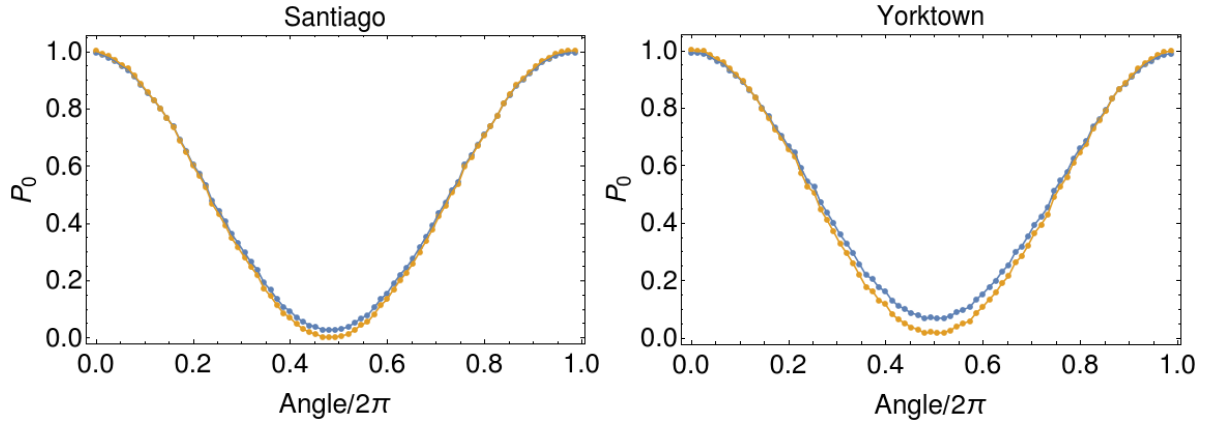


Figure 3.3: Single qubit calibration on Santiago and Yorktown. Here the blue (orange) line corresponds to the data without (with) readout correction.

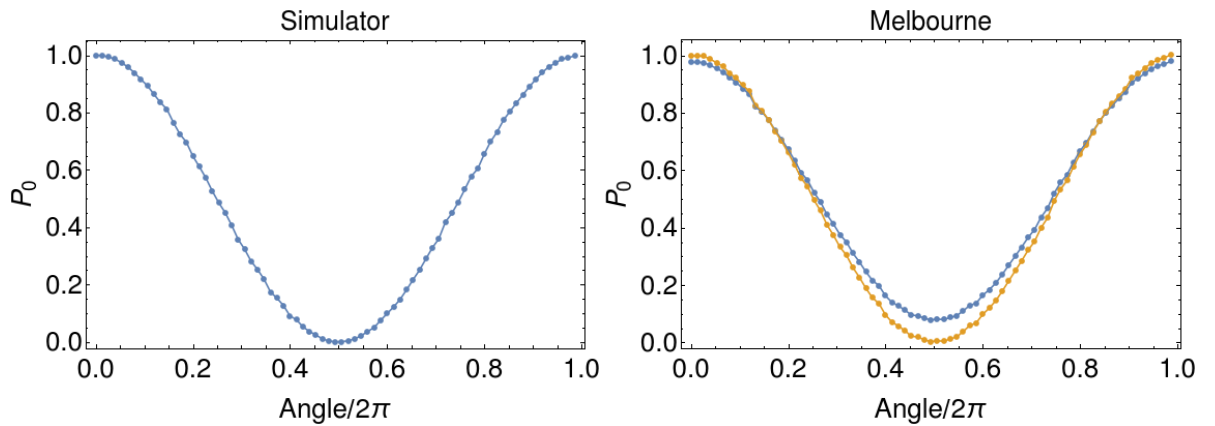


Figure 3.4: Single qubit calibration on Simulator and Melbourne. Here the blue (orange) line corresponds to the data without (with) readout correction. For the Simulator there is a single blue line since results do not require correction.

3.4. Software and hardware details

We have used the quantum systems freely available on Quantum Inspire [9] and IBM Quantum Experience [7]. More specifically, we have used the following backends:

- Spin-2 (Quantum Inspire), only for the EPCQCM;
- Starmon-5 (Quantum Inspire);
- Athens (IBM Quantum Experience);
- Ourense (IBM Quantum Experience);
- Santiago (IBM Quantum Experience);
- Valencia (IBM Quantum Experience);
- Vigo (IBM Quantum Experience);
- Yorktown (IBM Quantum Experience).

All the quantum systems but Spin-2 are 5-qubit processors based on superconducting qubits. Spin-2, on the other hand, is a 2-qubit processor based on spin qubits in silicon.

For Spin-2 and Starmon-5 we have implemented the experiments using the API provided by Quantum Inspire. For all the other backends, we have used Qiskit [1].

It should be mentioned that we had no control on the used hardware nor on the access to it. We used the publicly available platforms without any priority.

We have ran each experiment the maximum number of times allowed by each backend. The maximum number of shots allowed is 4096 for Spin-2, 16384 for Starmon-5 and 8192 for all the other backends. This means that even if we had a perfect quantum computer, the results would still be affected by a statistical uncertainty. More specifically, each measurement can be considered a Bernoulli trial, where the success probability corresponds to the probability p of measuring 0, which is also the fidelity F of the copy. The standard deviation of the Bernoulli distribution with success probability p is:

$$\sigma_{\text{Bernoulli}} = \sqrt{p(1-p)} = \sqrt{F(1-F)}.$$

If we are repeating the same experiment N times (i.e. the maximum number of shots allowed), we expect the standard deviation to be:

$$\sigma_{\text{stat}}^{(N)} = \frac{\sigma_{\text{Bernoulli}}}{\sqrt{N}} = \sqrt{\frac{F(1-F)}{N}}. \quad (3.10)$$

We can calculate this standard deviation in all the different cases we are going to consider. For the UQCM ($F = \frac{5}{6}$), the expected standard deviation is:

$$\sigma_{\text{stat}}^{(4096)} \approx 0.0058, \quad \sigma_{\text{stat}}^{(8192)} \approx 0.0041, \quad \sigma_{\text{stat}}^{(16384)} \approx 0.0029. \quad (3.11)$$

For the PCQCM and for the EPCQCM ($F = \frac{1}{2} + \frac{1}{2\sqrt{2}}$) we expect:

$$\sigma_{\text{stat}}^{(4096)} \approx 0.0055, \quad \sigma_{\text{stat}}^{(8192)} \approx 0.0039, \quad \sigma_{\text{stat}}^{(16384)} \approx 0.0028. \quad (3.12)$$

If we consider the uncertainties up to the first significant digit, there is no difference between the two cases.

This is the dispersion of the results that we would expect even if we had an ideal QCM, given the finite sampling. If we want to verify whether a QCM copies equally well certain input states, we should take into account this statistical uncertainty. If the standard deviation of our results is compatible with the one calculated above, we can assume that the quality of the copies is state-independent. Note that this does not mean that the copies are as good as theoretically possible: it could be that a QCM copies all the states 'equally bad'.

4

Results

In this section we list and discuss the results obtained. It is worth mentioning that calibrations and/or modifications of the quantum processors might change significantly the results obtained here.

NB: COMPARISON WITH OTHER EXPERIMENTAL RESULTS?

<https://arxiv.org/pdf/1909.03170.pdf> UQCM with gates (not peer-reviewed, but it has some review of modern experimental results)

<https://link.aps.org/doi/10.1103/PhysRevLett.88.187901> UQCM with NMR (bad results)

<https://science-sciencemag-org.tudelft.idm.oclc.org/content/296/5568/712> (photons)

<https://arxiv.org/pdf/quant-ph/0311010.pdf> economical phase covariant with NMR

4.1. Universal quantum cloning machine

4.1.1. Sphere

In Sec. 2 we found that the UQCM returns a fidelity of $F = 5/6$ for all the states in the Bloch sphere. The results that we found are summarized in Table 4.1.

	Starmon-5	Athens	Ourense	Santiago	Valencia	Vigo	Yorktown
F_1			0.777	0.777	0.752	0.687	0.752
σ_{F_1}			0.029	0.025	0.091	0.036	0.025
F_2			0.771	0.732	0.724	0.714	0.762
σ_{F_2}			0.035	0.030	0.064	0.068	0.017

Table 4.1: Average fidelity and corresponding standard deviation on the whole Bloch sphere for the two copies on each backend. The results are corrected with readout calibration.

In general, we find that the first copy performs better than the second one for all the cases. Also, the fidelity is lower than the expected one, and even lower than other copy machines (as will be discussed later), which are supposed to be worse. The standart deviations are close to the theoretical expectation. We found that the backend that have the highest fidelities is Ourense from IBM. The backend with the lowest standart deviation is Yorktown from IBM. We attirbute the later to the connectivity found in this device, which maps ideally the one of the UQCM. Nevertheless, this circuit is has a high cost of CNOT gates, which significantly increases the error in the fidelity.

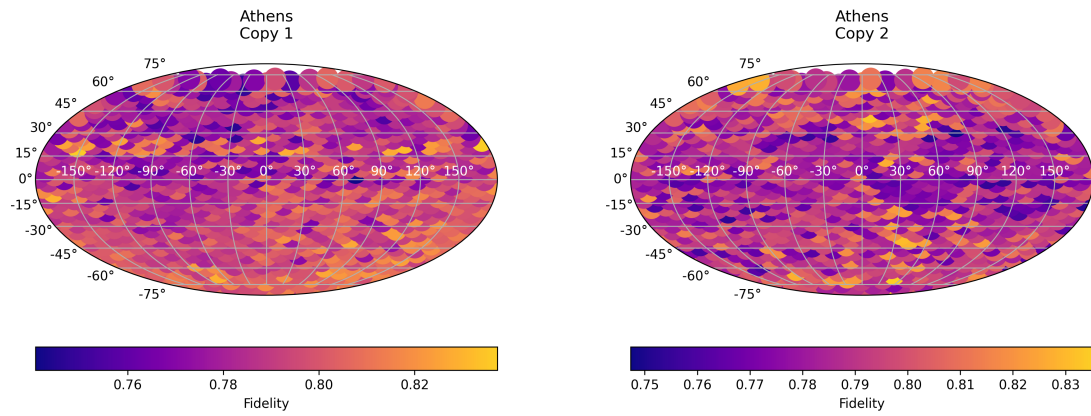


Figure 4.1: Fidelity sampled over the Bloch sphere using the UQCM implemented on Athens using readout correction.

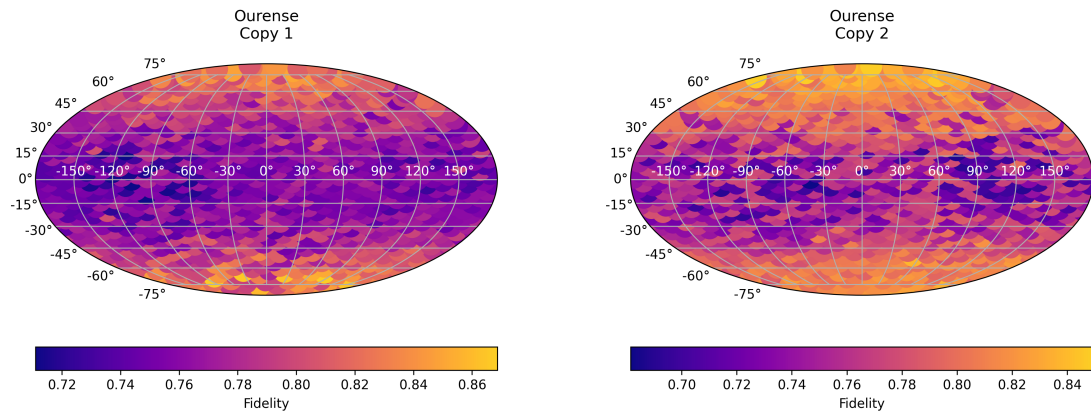


Figure 4.2: Fidelity sampled over the Bloch sphere using the UQCM implemented on Ourense using readout correction.

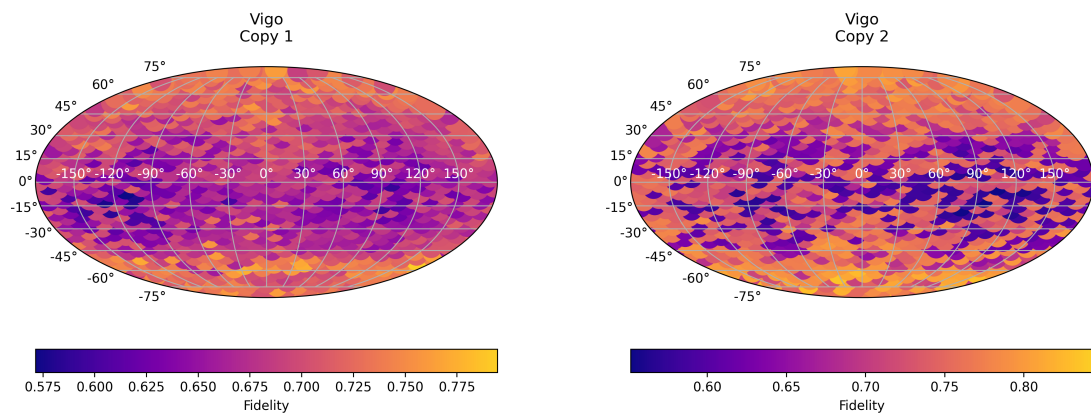


Figure 4.3: Fidelity sampled over the Bloch sphere using the UQCM implemented on Vigo using readout correction.

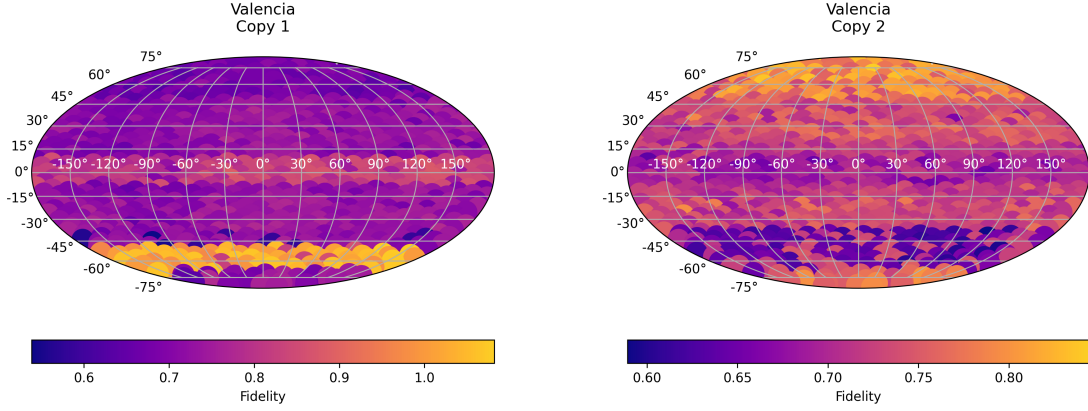


Figure 4.4: Fidelity sampled over the Bloch sphere using the UQCM implemented on Valencia using readout correction.

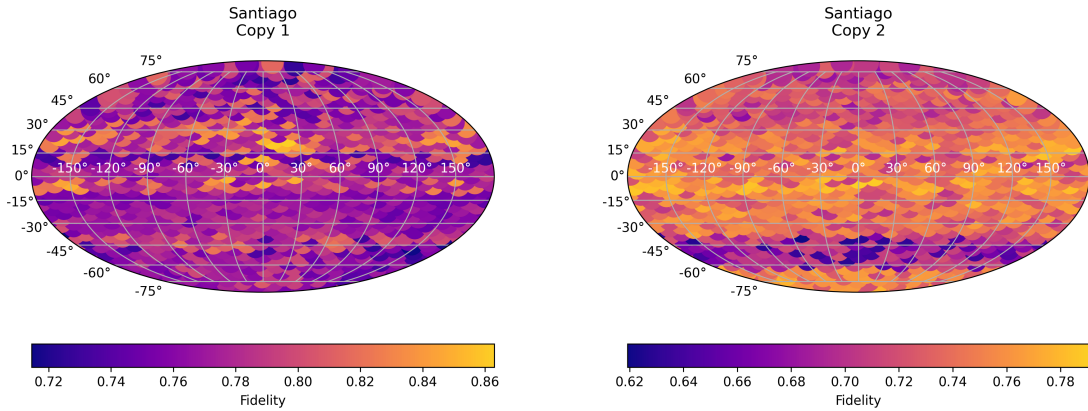


Figure 4.5: Fidelity sampled over the Bloch sphere using the UQCM implemented on Santiago using readout correction.

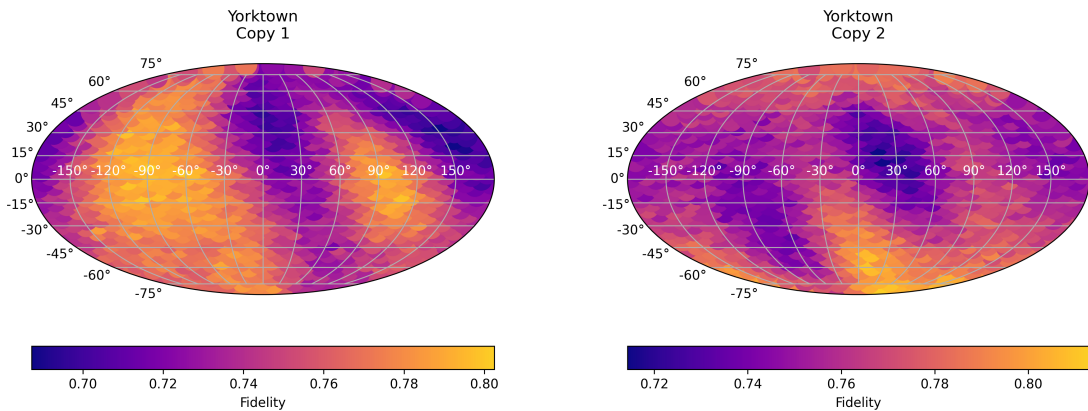


Figure 4.6: Fidelity sampled over the Bloch sphere using the UQCM implemented on Yorktown using readout correction.

We are not expecting any recognizable pattern in the Bloch sphere since the fidelity should be equal for all single qubit states. This is the case for most of the backends. We found an almost uniform sampling along the equatorial region as shown in Figs. 4.1, 4.2, 4.5, 4.4. In Fig. 4.6 we find a recognizable pattern which improves the fidelity along the axis of the Bloch sphere. We may attribute this to the internal working of the Yorktown machine rather than to any specific feature of the circuit.

For completeness, we include the results without the readout correction in Table 4.2. We can appreciate that the values have slightly changed. In general, we find that the readout correction improves the fidelity of one of the two copies, while decreases the fidelity of the other copy. We do not expect always an improvement, but a results closer to the real output of the machine, which already includes errors from other sources during the execution.

	Starmon-5	Athens	Ourense	Santiago	Valencia	Vigo	Yorktown
F_1			0.777	0.777	0.752	0.687	0.752
σ_{F_1}			0.029	0.025	0.091	0.036	0.025
F_2			0.771	0.732	0.724	0.714	0.762
σ_{F_2}			0.035	0.030	0.064	0.068	0.017

Table 4.2: Average fidelity and corresponding standard deviation on the whole Bloch sphere for the two copies on each backend. The results are not corrected with readout calibration.

4.1.2. Equator

For a sample of 100 points along the xz equator of the Bloch sphere we run the UQCM and obtain the results listed in Table 4.3. We found that the fidelity has improved with respect to the full sphere case for both copies. Since the fidelity presented here is an average over all the sampled points, it is not expected to have an improvement with respect to the previous case. Nevertheless, preparing the qubit in a state along the equator involves less operations than preparing it in an arbitrary state. Then, it is possible to expect an improvement in the fidelities.

	Starmon-5	Athens	Ourense	Santiago	Valencia	Vigo	Yorktown
F_1	0.747	0.792	0.790			0.729	0.737
σ_{F_1}	0.026	0.016	0.031			0.033	0.020
F_2	0.719	0.793	0.795			0.736	0.763
σ_{F_2}	0.039	0.020	0.036			0.074	0.020

Table 4.3: Average fidelity and corresponding standard deviation on the xz equator of the Bloch sphere for the two copies on each backend. The results are corrected with readout calibration.

In the following figures, we observe the fidelity of the states along the equator. We found that the fidelity of these states has a oscillatory behaviour. We expect it to be uniform, as is the case for Athens in Fig. 4.9. However, most of the previous figures show a clear oscillatory pattern. We attribute this behaviour to the error induced during the preparation of the states.

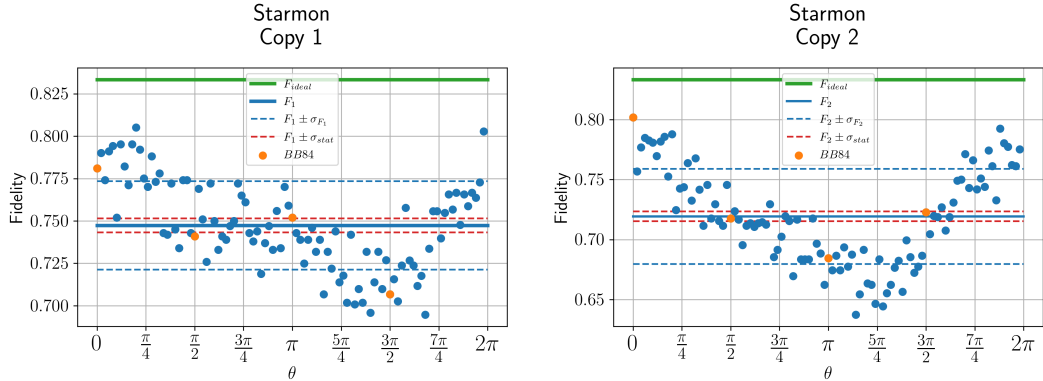


Figure 4.7: Fidelity sampled over the xz -equator using the UQCM implemented on Starmon-5 using readout correction. The solid green line is the expected fidelity, the solid blue line is the measured average fidelity, the dashed red lines indicate the expected dispersion and the dashed blue line indicate the measured dispersion. The orange points are the BB84 states.

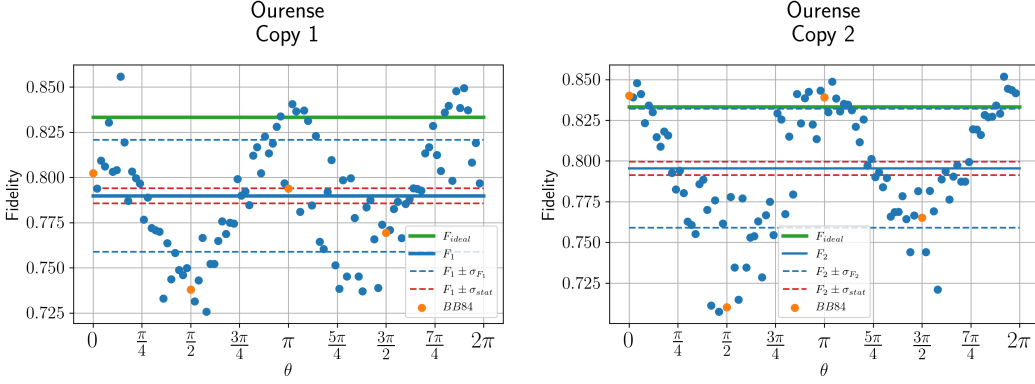


Figure 4.8: Fidelity sampled over the xz -equator using the UQCM implemented on Ourense using readout correction. The solid green line is the expected fidelity, the solid blue line is the measured average fidelity, the dashed red lines indicate the expected dispersion and the dashed blue line indicate the measured dispersion. The orange points are the BB84 states.

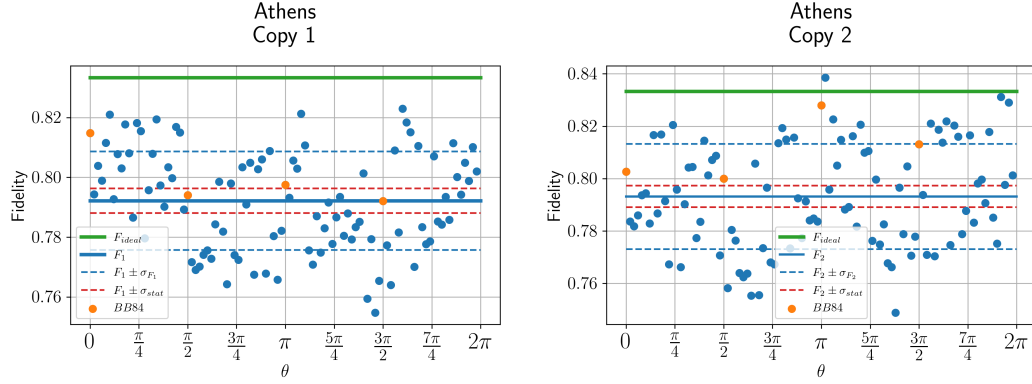


Figure 4.9: Fidelity sampled over the xz -equator using the UQCM implemented on Athens using readout correction. The solid green line is the expected fidelity, the solid blue line is the measured average fidelity, the dashed red lines indicate the expected dispersion and the dashed blue line indicate the measured dispersion. The orange points are the BB84 states.

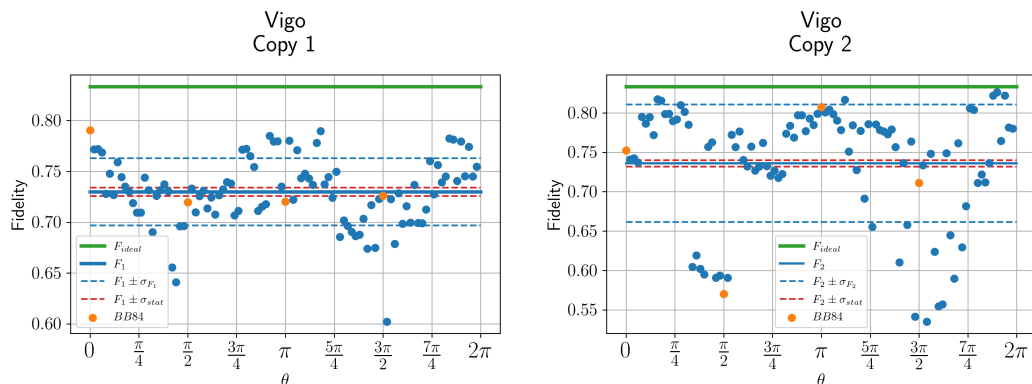


Figure 4.10: Fidelity sampled over the xz -equator using the UQCM implemented on Vigo using readout correction. The solid green line is the expected fidelity, the solid blue line is the measured average fidelity, the dashed red lines indicate the expected dispersion and the dashed blue line indicate the measured dispersion. The orange points are the BB84 states.

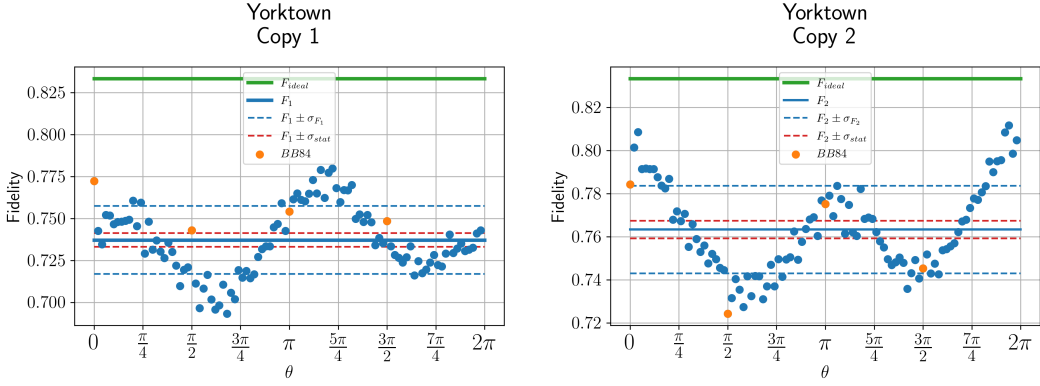


Figure 4.11: Fidelity sampled over the xz -equator using the UQCM implemented on Yorktown using readout correction. The solid green line is the expected fidelity, the solid blue line is the measured average fidelity, the dashed red lines indicate the expected dispersion and the dashed blue line indicate the measured dispersion. The orange points are the BB84 states.

For completeness, we include the results without the readout correction. The results are shown in Table 4.4. As before, we find that the readout improves the readout in few cases, e.g. Athens, and it decreases in most of them. The results are within the statistical uncertainty attributed to the finite sampling.

	Starmon-5	Athens	Ourense	Santiago	Valencia	Vigo	Yorktown
F_1	0.741	0.793	0.788			0.741	0.748
σ_{F_1}	0.025	0.016	0.029			0.030	0.018
F_2	0.721	0.794	0.790			0.743	0.762
σ_{F_2}	0.038	0.019	0.036			0.070	0.019

Table 4.4: Average fidelity and corresponding standard deviation on the xz equator of the Bloch sphere for the two copies on each backend. The results are not corrected with readout calibration.

4.1.3. BB84 States

We have sampled the BB84 states corresponding to the states pointing along the X and Z axis of the Bloch sphere. The results are shown in Table 4.5 with readout correction, and in Table 4 without it. We omitted the graphics since the can be found as orange points in the graphics of the UCQM sampled along the equator.

	Starmon-5	Athens	Ourense	Santiago	Valencia	Vigo	Yorktown
F_1	0.755		0.837		0.690	0.730	0.760
σ_{F_1}	0.035		0.040		0.034	0.0475	0.012
F_2	0.720		0.765		0.690	0.735	0.761
σ_{F_2}	0.041		0.065		0.045	0.052	0.026

Table 4.5: Average fidelity and corresponding standard deviation on the BB84 states for the two copies on each backend. The results are corrected with readout calibration.

We observe that in most of the cases the fidelity is decreased by the readout correction. We found that Ourense performs the best for a copy of the BB84 states, while Vigo is the worst. These features are attributed to the details of each specific device. Nevertheless they would be suitable to simulate a noisy channel where the copied qubit has decreased its fidelity to the values presented here.

	Starmon-5	Athens	Ourense	Santiago	Valencia	Vigo	Yorktown
F_1	0.755		0.835		0.690	0.762	0.772
σ_{F_1}	0.034		0.038		0.027	0.040	0.011
F_2	0.719		0.777		0.699	0.742	0.764
σ_{F_2}	0.039		0.057		0.042	0.049	0.026

Table 4.6: Average fidelity and corresponding standard deviation on the BB84 states for the two copies on each backend. The results are not corrected with readout calibration.

4.2. Phase covariant quantum cloning machine

4.2.1. Sphere

In Chapter 2, we found that the expected average fidelity and the associated standard deviation on the whole Bloch sphere are (see Equation 2.18 and Equation 2.19):

$$\bar{F} \approx 0.819, \quad \sigma_F \approx 0.031.$$

The results we found are summarized in Table 4.7 (corrected with readout calibration).

	Starmon-5	Athens	Ourense	Santiago	Valencia	Vigo	Yorktown
F_1	0.774	0.779	0.802	0.796	0.800	0.801	0.794
σ_{F_1}	0.041	0.036	0.031	0.035	0.040	0.035	0.025
F_2	0.766	0.823	0.780	0.773	0.791	0.807	0.755
σ_{F_2}	0.041	0.031	0.034	0.045	0.034	0.036	0.042

Table 4.7: Average fidelity and corresponding standard deviation on the whole Bloch sphere for the two copies on each backend. The results are corrected with readout calibration.

It is possible to observe that, on average, the PCQCM performs better than the UQCM, even if theoretically it should perform worse. As mentioned in Chapter 2, this is because the PCQCM circuit is much simpler than the UQCM one. The dispersion of the results is close to the expected one, however the average fidelity is lower than the ideal one (with the exception of the fidelity of the second copy for Athens). This suggests that the expected fidelity of the ideal PCQCM on the Bloch sphere is lowered more or less equally across the Bloch sphere, so that the qualitative pattern is preserved. Indeed, in the pictures below, it is possible to observe that the xz -equator performs better than the rest of the two hemispheres (the darker lobes).

In the following we report the projection of the results obtained on the Bloch sphere, corrected with the readout calibration (the non-corrected results can be observed in the appendix). In general, we can see the expected pattern for the fidelity. In certain cases, for example for Starmon-5 (Figure 4.12), the results are not symmetric: the region around $|-\rangle$ (i.e. the left lobe) is copied better than the region around $|+\rangle$ (i.e. the right lobe) on both the qubits (this happens in both the copies). Sometimes, for example looking at the results for Santiago (Figure 4.15), it is possible to observe some sudden discontinuities. These artefacts, present both in the corrected and the non-corrected results, correspond to one batch of circuits (on the IBM backends it is possible to group 75 circuits together). This could be due to the fact that two subsequent batches of circuits could be run hours apart, depending on the length of the queue. Therefore, it should not be assumed that the condition and the calibration of the quantum processors are the same throughout the sampling. The quality of the results could be improved if we could run all the circuits together. Finally, we observe again that the results obtained on Yorktown (4.18) are quite different compared to the others, even if in this case the connectivity of the quantum processor should not play a role.

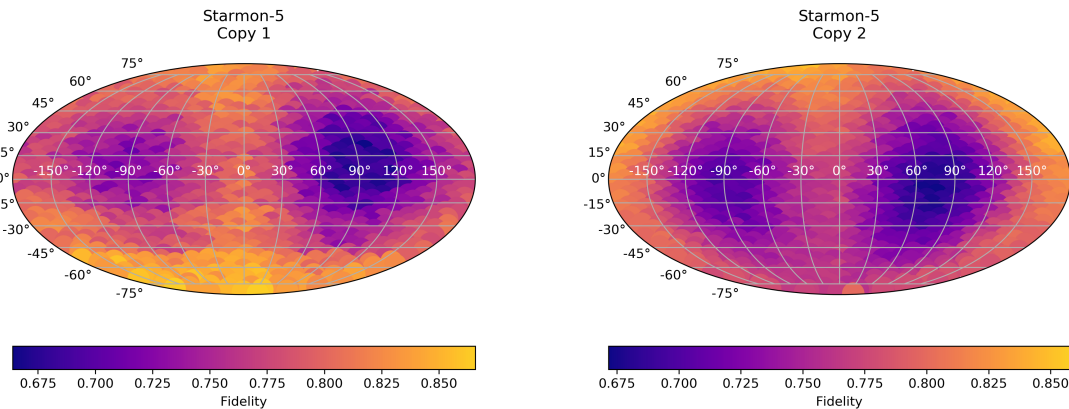


Figure 4.12: Fidelity sampled over the Bloch sphere using the PCQCM implemented on Starmon-5 using readout correction.

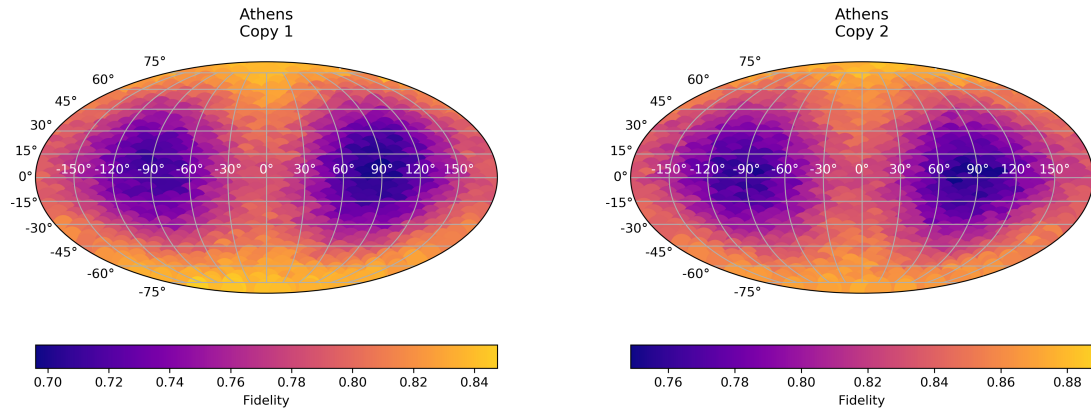


Figure 4.13: Fidelity sampled over the Bloch sphere using the PCQCM implemented on Athens using readout correction.

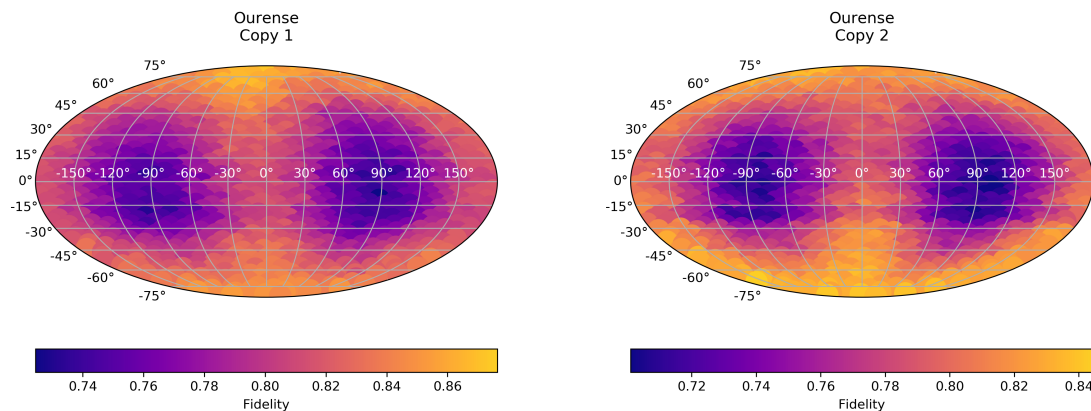


Figure 4.14: Fidelity sampled over the Bloch sphere using the PCQCM implemented on Ourense using readout correction.

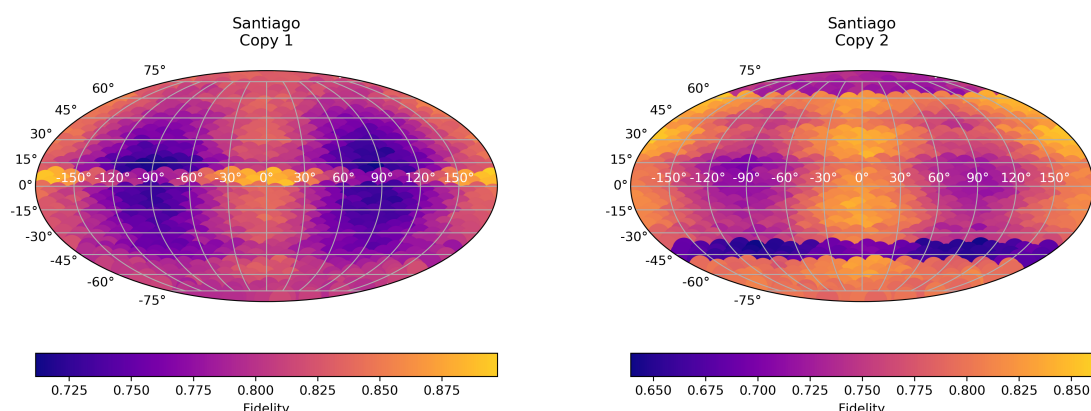


Figure 4.15: Fidelity sampled over the Bloch sphere using the PCQCM implemented on Santiago using readout correction.

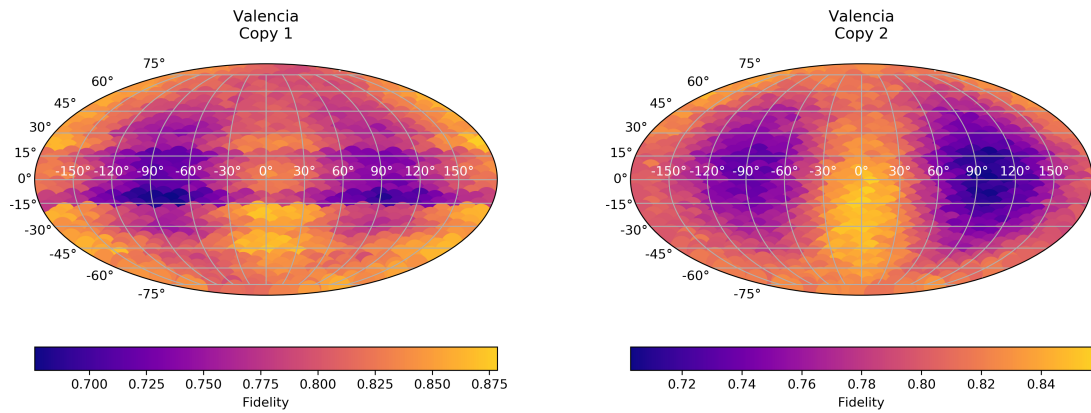


Figure 4.16: Fidelity sampled over the Bloch sphere using the PCQCM implemented on Valencia using readout correction.

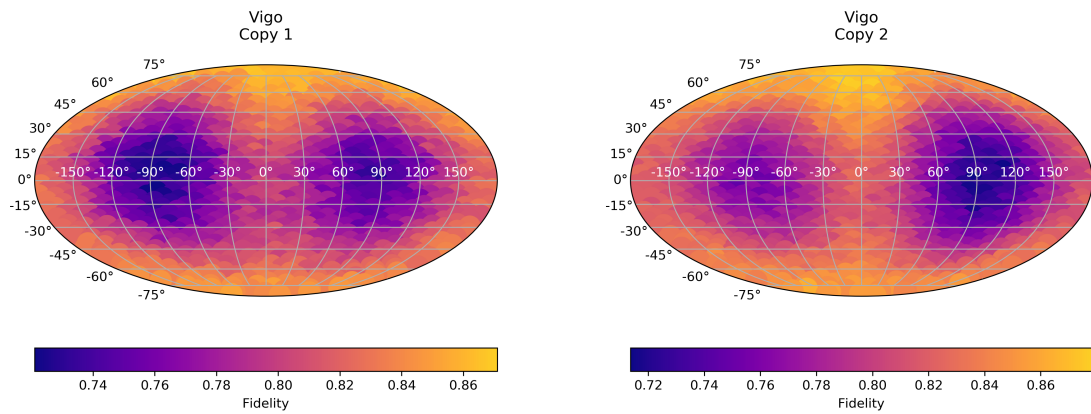


Figure 4.17: Fidelity sampled over the Bloch sphere using the PCQCM implemented on Vigo using readout correction.

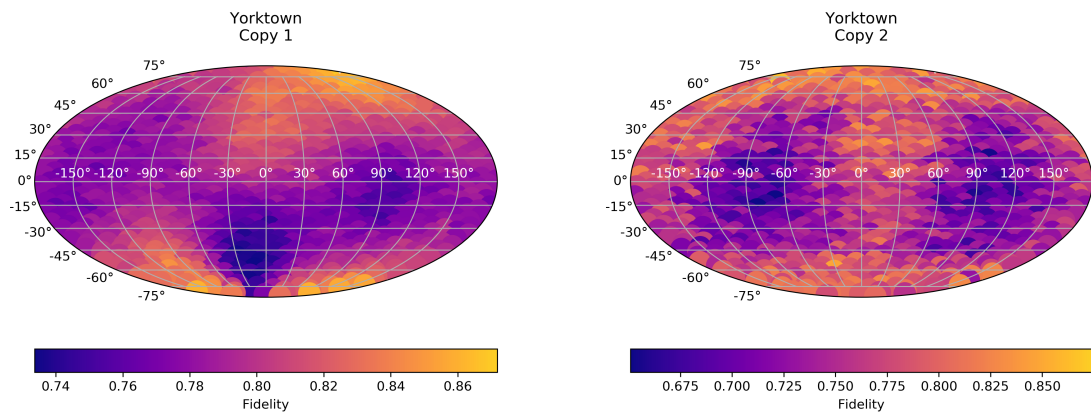


Figure 4.18: Fidelity sampled over the Bloch sphere using the PCQCM implemented on Yorktown using readout correction.

We conclude the analysis for the full sphere reporting also the results without readout correction.

	Starmon-5	Athens	Ourense	Santiago	Valencia	Vigo	Yorktown
F_1	0.761	0.782	0.801	0.788	0.768	0.784	0.794
σ_{F_1}	0.036	0.035	0.029	0.032	0.044	0.030	0.023
F_2	0.757	0.825	0.779	0.772	0.797	0.807	0.793
σ_{F_2}	0.038	0.030	0.033	0.043	0.030	0.035	0.009

Table 4.8: Average fidelity and corresponding standard deviation on the whole Bloch sphere for the two copies on each backend. The results are not corrected with readout calibration.

As discussed in the previous section for the UQCM, the readout calibration corrects a classical error associated to a measurement. Therefore, we expect the measured fidelity to be more accurate, but not necessarily closer to the ideal case. Indeed, sometimes the readout correction increases the fidelity and sometimes it decreases it.

4.2.2. Equator

The fidelity for the copies of equatorial states using an ideal PCQCM is (see Equation 2.17):

$$F = \frac{1}{2} + \frac{1}{2\sqrt{2}} \approx 0.854.$$

All the states should be copied equally well. However, we still expect a dispersion of the results because of the finite sampling (we are using 16384 shots for each input state for Starmon-5 and 8192 for the IBM backends). As discussed previously in Chapter 3, the expected statistical uncertainty is (see 3.12):

$$\sigma_{stat}^{(8192)} \approx 0.004, \quad \sigma_{stat}^{(16384)} \approx 0.003.$$

If the dispersion of the results is significantly greater than the expected one, it means that the states are not copied equally well.

The results we found are summarized in Table 4.9 (corrected with readout calibration).

	Starmon-5	Athens	Ourense	Santiago	Valencia	Vigo	Yorktown
F_1	0.817	0.814	0.839	0.825	0.834	0.836	0.804
σ_{F_1}	0.014	0.019	0.018	0.014	0.023	0.022	0.030
F_2	0.815	0.858	0.811	0.857	0.836	0.839	0.819
σ_{F_2}	0.027	0.015	0.015	0.018	0.019	0.022	0.034

Table 4.9: Average fidelity and corresponding standard deviation on the xz -equator for the two copies on each backend. The results are corrected with readout calibration.

The average fidelity has significantly increased compared to the sampling on the whole sphere (and of course compared to the UQCM). In several cases the fidelity is greater than the bound of the UQCM (i.e. $F \approx 0.833$). The average fidelity of the second copy of Athens and Santiago achieves the theoretical bound for the PCQCM (i.e. $F \approx 0.854$).

However, the measured dispersion of the results is significantly greater than the statistical uncertainty in every backend. This means that we can not conclude that all the input states on the xz -equator are copied equally well. This can be more clearly seen in the pictures below, where we have reported the measured fidelity of each input state.

There is a recurring pattern occurring in several backends, for example Athens (see Figure 4.20): moving across the equator, the fidelity oscillates. There is a peak around $|0\rangle$ and $|1\rangle$ and a dip around $|+\rangle$ and $|-\rangle$. For Vigo (see 4.21) the oscillating pattern is not symmetric (the dips and the peaks are not at the same height). For Valencia (see 4.23) the oscillating pattern is translated: the peaks are around $|+\rangle$ and $|-\rangle$, whereas the dips are around $|0\rangle$ and $|1\rangle$. In all these cases, the patterns are consistent with the results obtained on xz -equator while sampling the full sphere. Considering, for example, the results for the second copy of Valencia in the right panel of Figure 4.16, it is possible to see a bright spot around $|+\rangle$ (exactly where we see the peak in Figure 4.23). For Santiago, we can again see the artefacts previously discussed. In this case they affect the last 25 points, which are significantly displaced with respect to the first 75. Finally, we observe that the results for the two copies of Yorktown are qualitatively different, as previously seen: the fidelity of the first copy has a clear dependence from the angle, whereas the second one is uniformly distributed around the average value.

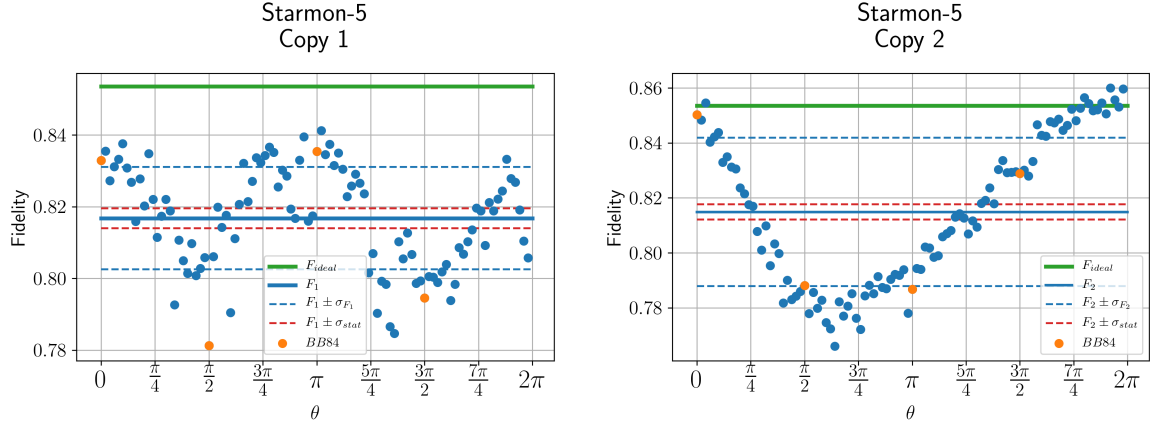


Figure 4.19: Fidelity sampled over the xz -equator using the PCQCM implemented on Starmon-5 using readout correction. The solid green line is the expected fidelity, the solid blue line is the measured average fidelity, the dashed red lines indicate the expected dispersion and the dashed blue line indicate the measured dispersion. The orange points are the BB84 states.

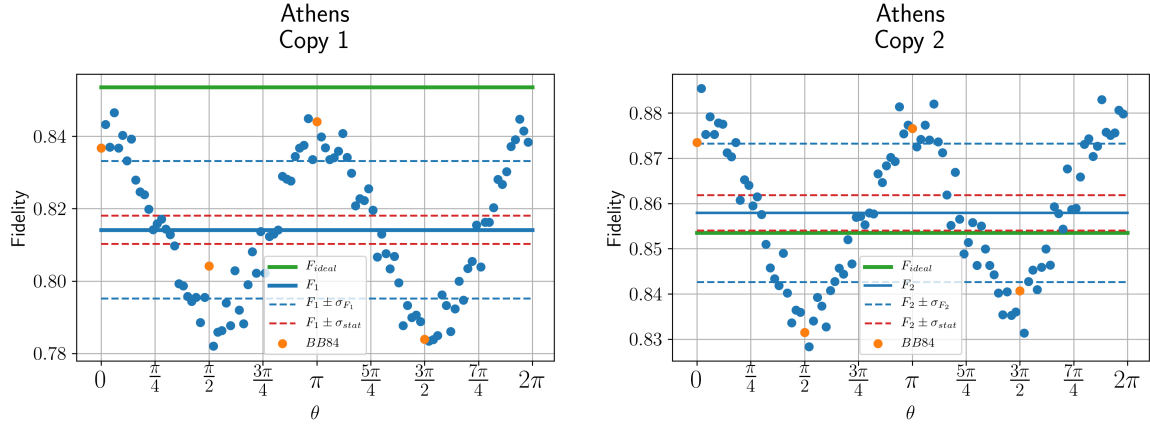


Figure 4.20: Fidelity sampled over the xz -equator using the PCQCM implemented on Athens using readout correction. The solid green line is the expected fidelity, the solid blue line is the measured average fidelity, the dashed red lines indicate the expected dispersion and the dashed blue line indicate the measured dispersion.

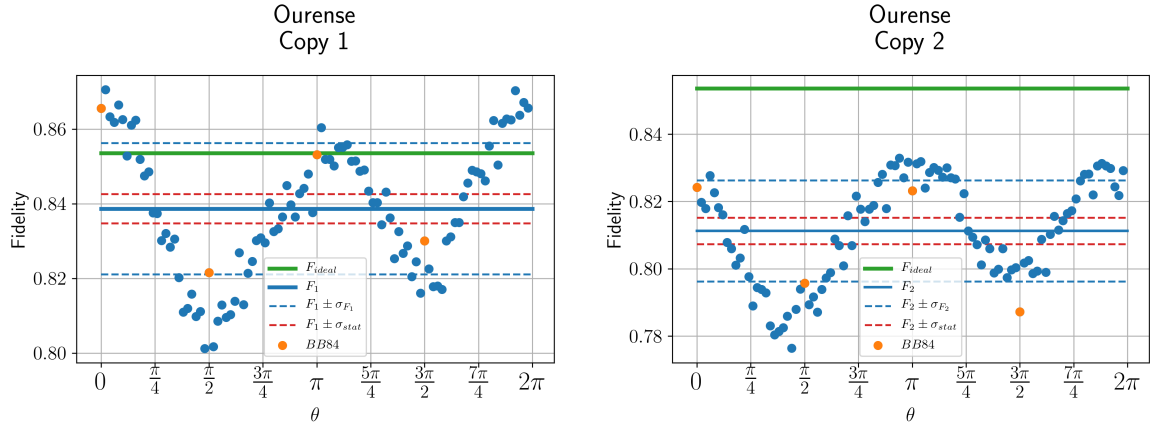


Figure 4.21: Fidelity sampled over the xz -equator using the PCQCM implemented on Ourense using readout correction. The solid green line is the expected fidelity, the solid blue line is the measured average fidelity, the dashed red lines indicate the expected dispersion and the dashed blue line indicate the measured dispersion.

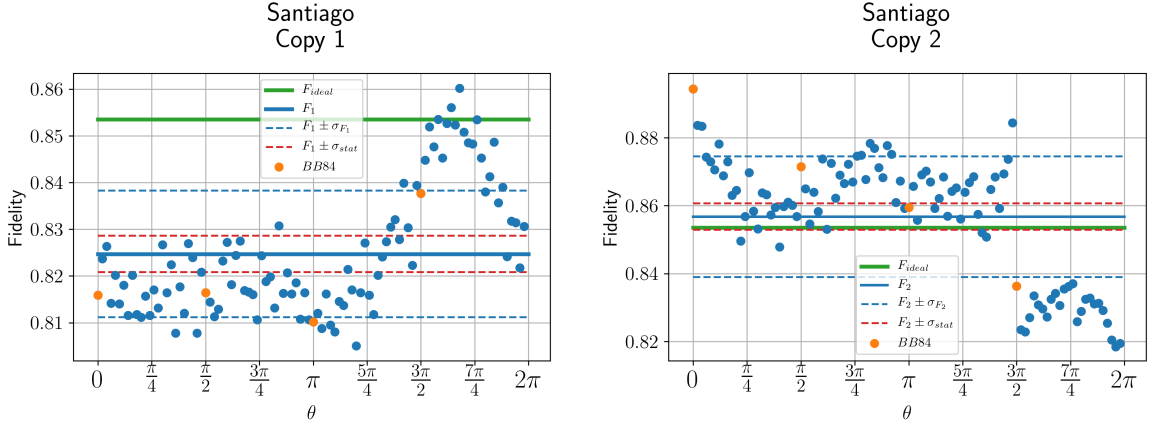


Figure 4.22: Fidelity sampled over the xz -equator using the PCQCM implemented on Santiago using readout correction. The solid green line is the expected fidelity, the solid blue line is the measured average fidelity, the dashed red lines indicate the expected dispersion and the dashed blue line indicate the measured dispersion.

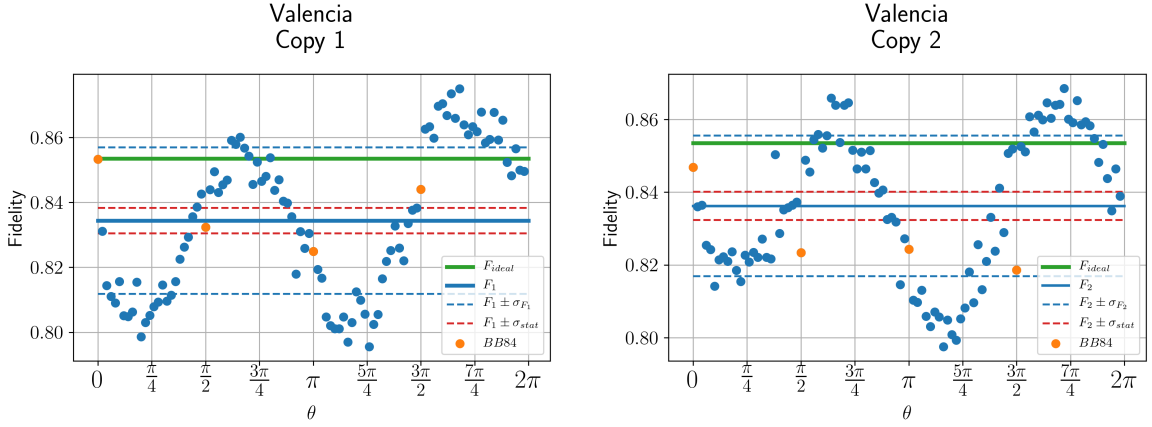


Figure 4.23: Fidelity sampled over the xz -equator using the PCQCM implemented on Valencia using readout correction. The solid green line is the expected fidelity, the solid blue line is the measured average fidelity, the dashed red lines indicate the expected dispersion and the dashed blue line indicate the measured dispersion.

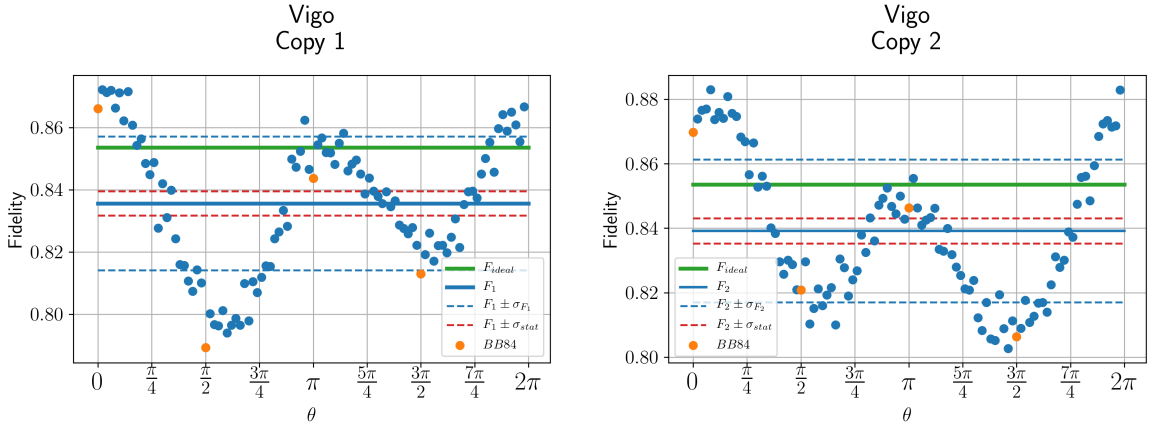


Figure 4.24: Fidelity sampled over the xz -equator using the PCQCM implemented on Vigo using readout correction. The solid green line is the expected fidelity, the solid blue line is the measured average fidelity, the dashed red lines indicate the expected dispersion and the dashed blue line indicate the measured dispersion.

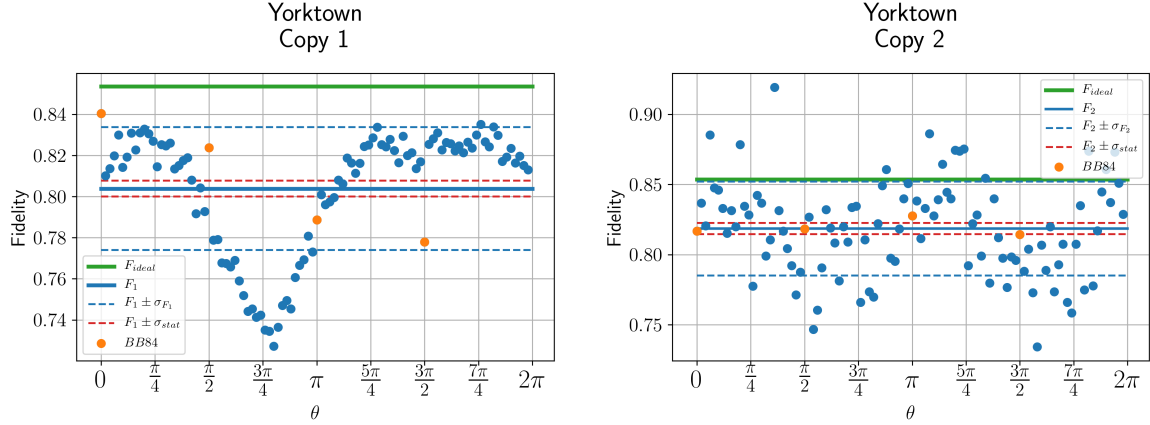


Figure 4.25: Fidelity sampled over the xz -equator using the PCQCM implemented on Yorktown using readout correction. The solid green line is the expected fidelity, the solid blue line is the measured average fidelity, the dashed red lines indicate the expected dispersion and the dashed blue line indicate the measured dispersion.

For the sake of completeness, we also report the non-corrected results.

	Starmon-5	Athens	Ourense	Santiago	Valencia	Vigo	Yorktown
F_1	0.807	0.817	0.836	0.822	0.820	0.798	0.802
σ_{F_1}	0.014	0.019	0.017	0.013	0.017	0.019	0.028
F_2	0.798	0.858	0.811	0.815	0.836	0.836	0.807
σ_{F_2}	0.025	0.015	0.015	0.011	0.018	0.021	0.008

Table 4.10: Average fidelity and corresponding standard deviation on the xz -equator for the two copies on each backend. The results are not corrected with readout calibration.

4.2.3. BB84 states

In Table 4.11 are presented the results obtained considering the BB84 states as input states, considering the readout correction. There is not a significant difference when comparing these results with the one obtained for the full equator. This is reasonable: since the BB84 states correspond to the peaks or dips of the fidelity on the equator discussed before, both the average and the standard deviation should remain more or less unchanged.

	Starmon-5	Athens	Ourense	Santiago	Valencia	Vigo	Yorktown
F_1	0.838	0.818	0.840	0.833	0.841	0.820	0.807
σ_{F_1}	0.027	0.023	0.022	0.011	0.009	0.031	0.028
F_2	0.808	0.852	0.817	0.833	0.820	0.830	0.788
σ_{F_2}	0.029	0.024	0.018	0.016	0.005	0.032	0.038

Table 4.11: Average fidelity and corresponding standard deviation for the BB84 for the two copies on each backend. The results are corrected with readout calibration.

We conclude the discussion of the results for the PCQCM with the results for the BB84 states without readout correction.

	Starmon-5	Athens	Ourense	Santiago	Valencia	Vigo	Yorktown
F_1	0.802	0.820	0.838	0.829	0.821	0.797	0.806
σ_{F_1}	0.024	0.023	0.021	0.011	0.008	0.026	0.027
F_2	0.796	0.853	0.815	0.832	0.824	0.829	0.793
σ_{F_2}	0.027	0.023	0.017	0.015	0.005	0.030	0.008

Table 4.12: Average fidelity and corresponding standard deviation for the BB84 for the two copies on each backend. The results are not corrected with readout calibration.

4.3. Economical phase covariant quantum cloning machine

4.3.1. Sphere

Without readout correction:

	Spin-2	Starmon-5	Athens	Ourense	Santiago	Valencia	Vigo	Yorktown
F_1	0.714	0.741	0.810	0.776	0.811	0.819	0.803	0.789
σ_{F_1}	0.128	0.142	0.142	0.159	0.132	0.132	0.112	0.129
F_2	0.690	0.788	0.812	0.834	0.794	0.826	0.802	0.777
σ_{F_2}	0.083	0.126	0.136	0.119	0.149	0.133	0.149	0.137

With readout correction:

	Spin-2	Starmon-5	Athens	Ourense	Santiago	Valencia	Vigo	Yorktown
F_1	0.731	0.753	0.810	0.777	0.814	0.820	0.824	0.781
σ_{F_1}	0.172	0.151	0.144	0.166	0.138	0.138	0.131	0.140
F_2	0.821	0.791	0.811	0.844	0.799	0.807	0.801	0.776
σ_{F_2}	0.130	0.133	0.139	0.127	0.153	0.153	0.154	0.145

4.3.2. Equator

Without readout correction:

	Spin-2	Starmon-5	Athens	Ourense	Santiago	Valencia	Vigo	Yorktown
F_1	0.751	0.784	0.839	0.813	0.837	0.852	0.824	0.819
σ_{F_1}	0.029	0.021	0.010	0.018	0.009	0.005	0.012	0.037
F_2	0.704	0.841	0.838	0.867	0.799	0.850	0.826	0.832
σ_{F_2}	0.025	0.022	0.009	0.019	0.022	0.012	0.018	0.026

With readout correction:

	Spin-2	Starmon-5	Athens	Ourense	Santiago	Valencia	Vigo	Yorktown
F_1	0.751	0.792	0.840	0.815	0.838	0.851	0.850	0.814
σ_{F_1}	0.042	0.022	0.011	0.019	0.010	0.005	0.014	0.041
F_2	0.862	0.846	0.837	0.879	0.811	0.832	0.828	0.835
σ_{F_2}	0.037	0.023	0.009	0.022	0.019	0.015	0.019	0.028

4.3.3. BB84 states

Without readout correction:

	Spin-2	Starmon-5	Athens	Ourense	Santiago	Valencia	Vigo	Yorktown
F_1	0.666	0.788	0.840	0.812	0.846	0.844	0.832	0.814
σ_{F_1}	0.018	0.024	0.008	0.027	0.008	0.003	0.017	0.027
F_2	0.765	0.845	0.842	0.866	0.831	0.848	0.827	0.833
σ_{F_2}	0.022	0.023	0.003	0.020	0.012	0.010	0.022	0.022

With readout correction:

	Spin-2	Starmon-5	Athens	Ourense	Santiago	Valencia	Vigo	Yorktown
F_1	0.823	0.801	0.841	0.815	0.851	0.858	0.850	0.809
σ_{F_1}	0.027	0.025	0.008	0.028	0.008	0.003	0.020	0.029
F_2	0.847	0.848	0.840	0.874	0.833	0.843	0.829	0.835
σ_{F_2}	0.041	0.024	0.003	0.021	0.012	0.011	0.023	0.023

5

Conclusions

More backends with different technologies. Thorough investigation on different choice of qubits.

A

Results without readout correction

A.1. Universal quantum cloning machine

A.2. Phase covariant quantum cloning machine

A.3. Economical phase covariant quantum cloning machine

Bibliography

- [1] Héctor Abraham et al. Qiskit: An open-source framework for quantum computing, 2019.
- [2] Dagmar Bruß, Mirko Cinchetti, G. Mauro D’Ariano, and Chiara Macchiavello. Phase-covariant quantum cloning. *Phys. Rev. A*, 62:012302, Jun 2000. doi: 10.1103/PhysRevA.62.012302. URL <https://link.aps.org/doi/10.1103/PhysRevA.62.012302>.
- [3] V. Bužek and M. Hillery. Quantum copying: Beyond the no-cloning theorem. *Phys. Rev. A*, 54:1844–1852, Sep 1996. doi: 10.1103/PhysRevA.54.1844. URL <https://link.aps.org/doi/10.1103/PhysRevA.54.1844>.
- [4] Thomas Durt and Jiangfeng Du. Characterization of low-cost one-to-two qubit cloning. *Phys. Rev. A*, 69:062316, Jun 2004. doi: 10.1103/PhysRevA.69.062316. URL <https://link.aps.org/doi/10.1103/PhysRevA.69.062316>.
- [5] Thomas Durt, Jaromír Fiurášek, and Nicolas J. Cerf. Economical quantum cloning in any dimension. *Phys. Rev. A*, 72:052322, Nov 2005. doi: 10.1103/PhysRevA.72.052322. URL <https://link.aps.org/doi/10.1103/PhysRevA.72.052322>.
- [6] Heng Fan, Keiji Matsumoto, Xiang-Bin Wang, and Miki Wadati. Quantum cloning machines for equatorial qubits. *Phys. Rev. A*, 65:012304, Dec 2001. doi: 10.1103/PhysRevA.65.012304. URL <https://link.aps.org/doi/10.1103/PhysRevA.65.012304>.
- [7] IBM. IBM Quantum Experience. URL <https://quantum-computing.ibm.com>.
- [8] Chi-Sheng Niu and Robert B. Griffiths. Two-qubit copying machine for economical quantum eavesdropping. *Phys. Rev. A*, 60:2764–2776, Oct 1999. doi: 10.1103/PhysRevA.60.2764. URL <https://link.aps.org/doi/10.1103/PhysRevA.60.2764>.
- [9] QuTech. Quantum Inspire Home. URL <https://www.quantum-inspire.com>.
- [10] Valerio Scarani, Sofyan Iblisdir, Nicolas Gisin, and Antonio Acín. Quantum cloning. *Rev. Mod. Phys.*, 77:1225–1256, Nov 2005. doi: 10.1103/RevModPhys.77.1225. URL <https://link.aps.org/doi/10.1103/RevModPhys.77.1225>.
- [11] W. K. Wootters and W. H. Zurek. A single quantum cannot be cloned. *Nature*, 299(5886):802–803, Oct 1982. ISSN 1476-4687. doi: 10.1038/299802a0. URL <https://doi.org/10.1038/299802a0>.